# Framework for Generating Failure Surface through Virtual Testing of Unidirectional Polymeric Composite

by

Yatin Bharat Parakhiya

A Thesis Presented in Partial Fulfillment
of the Requirements for the Degree
Master of Science

Approved April 2020 by the
Graduate Supervisory Committee:

Subramaniam Rajan, Chair
Barzin Mobasher
Christian Hoover

ARIZONA STATE UNIVERSITY

August 2020

ABSTRACT

A framework to obtain the failure surface of a unidirectional composite which can be used as an input for Generalized Tabulated Failure Criterion in MAT_213 – an orthotropic elasto-plastic material model implemented in LS-DYNA, a commercial finite element program, is discussed in this research. A finite element model consisting of the fiber and the matrix is generated using the Virtual Testing Software System (VTSS) developed at Arizona State University (ASU). The framework is illustrated using the T800-F3900 unidirectional composite material manufactured by Toray Composites. The T800S fiber is modeled using MAT_213. The F3900 matrix phase is modeled using MAT_187-SAMP1. The response of the virtual tests in 1-direction tension, 1-direction compression, 2-direction tension, 2-direction compression and 2-1 plane shear are verified against the results obtained from experiments performed under quasi-static and room temperature conditions (QS-RT). Finally, a roadmap to generate the failure surface using virtual test is proposed.

# DEDICATION

To my family, friends, colleagues and teachers who have always been supportive throughout my studies.

ACKNOWLEDGMENTS

I would like to thank Dr. Rajan for his mentorship and guidance as my Committee Chair. I would also like to thank Dr. Hoover and Dr. Mobasher for serving as committee members and for the teaching they provided. I would like to thank Dr. Bilal Khaled and Loukham Shyamsunder for their guidance and mentorship.

TABLE OF CONTENTS

Page

Page

LIST OF TABLES

Table Page

LIST OF FIGURES

Figure Page

Figure Page

Figure Page

# CHAPTER 1

# INTRODUCTION

Composites are widely used in the automobile and aerospace industries due to their high strength to weight ratio, and the ability to customize the material properties to achieve required strength. They are widely used in structural components where resistance to impact is critical. Sophisticated finite element analysis (FEA) programs like LS-DYNA [1] are used in the design of these components by simulating impact events through rigorous modeling. The accuracy of the predictive capability of these models under impact events significantly depends on the accuracy of the material models.

A generalized orthotropic elasto-plastic material model implemented as MAT_213 in LS-DYNA can simulate the deformation, damage and failure of the composites. MAT_213 was developed as a response to observed weaknesses in current composite material models and seeks to improve upon them. The details of MAT_213 theory, implementation, and verification and validation can be found in several publications [2] [3] [4] [5]. One of the key features of this material model is the use of tabulated input for stress-strain, damage and failure data in different material directions, thus giving the user a wide latitude in defining a variety of behavior difficult to capture otherwise.

Accurate prediction of deformation, damage and failure is important while designing components that undergo large deformations, damage and total or partial failure during impact events. The failure of composites has been studied at various spatial scales. Examples include Hashin's failure criterion which is a stress based polynomial [6], Puck's failure

criterion based on Mohr-Coulomb model [7], and Gosse and Christensen failure criterion based on strain invariant failure theory [8]. Most of the existing failure models often require complex tests to characterize the model parameters and yet may not be completely able to predict the failure of the composite [9]. The macroscale or the structural level failure of composites can be attributed to the combination and interaction of various failure mechanisms occurring at the microscale and the mesoscale. This likely leads to the failure envelope (that is typically a function of stresses or strains) that may not conform to a particular mathematical shape but rather can have an arbitrary shape. To help define an arbitrarily shaped failure envelope, a different methodology is proposed where a user-defined, tabulated failure surface is used to help predict the failure of the composites [10]. A combination of mechanical testing and numerical experiments (virtual testing) can be used for generating the failure surface of a composite under multi-axial state of stress.

The mechanical testing approach under multi-axial stress state is often expensive and complex for a variety of reasons-special fixtures may be required to hold the specimen, prevent specimen from buckling, free edge effects, and failure near the grips due to stress concentrations. In the virtual testing approach, these experimental challenges can be minimized and sometimes, eliminated. Hence, numerical micro-mechanical analysis is widely used for predicting the deformation, damage and failure of the composite under multi-axial stress state [11] [12] [13]. One of the advantages of virtual testing is that it not only overcomes some of the challenges of laboratory testing but also provides insights into microscopic behavior of a composite that can be linked to its macroscopic behavior. An example of this alternate path is the work by Totry et al. [11], where virtual testing is used for

generating failure locus of carbon-fiber/epoxy composite under combined transverse compression and out-of-plane shear state since mechanical testing of the composite for this biaxial stress state is highly complex.

There are different approaches to building and using a representative unit cell (RUC) for micro-mechanical analysis of a composite. A simple but elegant approach is to use an array of repeating unit cells with the goal of generating a model that mimics the laboratory test specimen as closely as possible [13]. In the virtual test models discussed in [13], both the fiber and the matrix were modeled separately and a perfect bond was assumed between them. The fiber was modeled as an elastic-transversely isotropic material and the matrix was modeled as an elastic-perfectly plastic material. Denoting the 1, 2 and 3- directions as the Principal Material Directions (PMD) of a unidirectional composite, the comparison of the virtual test results obtained from this approach for the T800/F3900[14], a unidirectional composite, in the 1-direction tension and 1-direction compression showed good agreement with the experimental results [15]. However, the 1-2 plane shear response of the virtual test was significantly stiffer while the plastic deformation in the matrix was captured in the 2-direction tension, the 2-direction compression and 1-2 plane shear tests, the plastic response was assumed to be dependent on shear yielding only. It is well known fact that the yielding of the epoxy is pressure dependent. The pressure dependence in addition to the shear yielding of the epoxy resin is attributed to the different yield stresses of the epoxy in uniaxial tension and compression [16]. Many researchers have modeled the behavior of the epoxy using Mohr-Coulomb elasto-plastic model [11] and Drucker-Prager elasto-plastic model [12]. Experimental studies [17] have shown that neither of these models capture the behavior of

the epoxy resin satisfactorily. MAT_187 is a material model in LS-DYNA developed for polymers based on experimental observations that show strain rate effects and damage on polymer behavior. In this material model, different yield surfaces like von-Mises, pressure dependent Drucker-Prager, $C^1$ differentiable yield surface or a piecewise linear yield surface in pressure and von-Mises space can be defined by selecting the appropriate input parameters [18].

In this research, validation of virtual test specimens is discussed in detail by comparing the virtual test predictions to the experimental data. The virtual test models that are constructed to be similar to the experimental specimens, are subjected to five in-plane tests, and their responses are verified against the available experimental data [19]. The five in-plane tests are 1-direction tension, 1-direction compression, 2-direction tension, 2-direction compression and 2-1 plane shear. The validation process is further divided into two steps:

1. In the first step, the fiber phase and the matrix phase are modeled with the fiber-matrix interface assumed to be a perfect bond. The fiber phase is modeled using MAT_213 and matrix phase is modeled using MAT_187. The deformation only response is verified against the QS-RT tests. The fiber properties used in MAT_213 are obtained through a combination of the available data from the manufacturer and inverse analysis of a composite similar to T800/F3900 [13]. In inverse analysis process, the fiber properties were chosen such that the computed composite response using micromechanical analysis through MAC/GMC code [20] matched the composite properties obtained by [21]. The T800 fiber is

modeled as linear-elastic and transversely isotropic with asymmetry in longitudinal tension and compression modulus. The longitudinal modulus of the fiber in compression is obtained through a simple linear interpolation technique. The virtual test response of the composite in 1-direction compression with two different longitudinal fiber moduli serving as the upper bound and the lower bound is compared with the QS-RT 1-direction compression response of the T800/F3900 composite. The virtual test stresses corresponding to a strain value of 0.003 are linearly interpolated with respect to the corresponding longitudinal compression modulus of the fiber to obtain the longitudinal compression modulus of the fiber at the targeted stress of the QS-RT experimental response corresponding to a strain value of 0.003. The details of the fiber properties are provided in section 4.1 of Chapter 4. The matrix properties used in MAT_187 are obtained from the experiments performed in unidirectional tension, unidirectional compression and Iosipescu shear, at ASU [22]. The material model parameter known as RBCFAC, ratio of biaxial compression to uniaxial compression, the virtual test responses of the composite in 2-direction compression with RBCFAC value ranging from 1.5 to 0.833 are compared against the experimental QS-RT responses and RBCFAC is chosen such that the virtual test response is close to the experimental response. The details of matrix properties are provided in section 4.2 of Chapter 4. The convergence analysis of the virtual tests considering only the deformation of the constituents and

excluding failure, is performed to check the effect of the calibrated fiber and matrix properties on the different tests and different meshes.

2. In the second step, the failure of the fiber and the matrix constituents are included in the virtual tests in addition to the modeling parameters obtained in the earlier step. The effect of the mesh on the deformation and the failure is studied via convergence analysis. Failure parameters of the constituent materials are calibrated using experimental results as guide. This step is required to correlate the failure of the constituents: fiber and matrix to the macroscopic failure of the composite

The focus of this research is to develop the basic framework that can then be used to generate the failure surface for a unidirectional composite, i.e. the T800/F3900 composite under in-plane state of stress and out-of-plane state of stress. The results from the virtual tests can be used to generate the tabulated input to drive the Generalized Tabulated Failure Criterion (GTFC) in MAT_213 [10]. The roadmap for generating the failure surface in in-plane state of stress is as follows:

1. Validate virtual test specimens using the five in-plane tests – 1-direction compression and tension, 2-direction compression and tension, and 2-1 plane shear.
2. Use a collection of RUCs to generate the virtual test specimen with appropriate boundary conditions suitable for different combinations of in-plane state of stress and generating the corresponding failure locus.

3. Convert the failure locus from stress and strain space to invariant ($r_{IP} - \theta_{IP}$) space suitable for input to drive GTFC in MAT_213.

Similarly, for generating the failure surface in the out-of-plane states of stress, the steps are as follows:

1. Validate virtual test specimens in 1-3 plane shear, 2-3 plane shear, and 3-direction tension and compression.
2. Use a collection of RUCs to generate the virtual test specimens with appropriate boundary conditions suitable for different combinations of out-of-plane state of stress and generating the corresponding failure locus.
3. Convert the failure locus from stress and strain space to invariant ($r_{OOP} - \theta_{OOP}$) space suitable for input to drive GTFC.

The thesis is divided into six chapters. In Chapter 2, an overview of MAT_213 is discussed with primary focus on the Generalized Tabulated Failure Criterion. The components of the virtual testing software system used for generating the virtual test specimens and post-processing the virtual test results are discussed in Chapter 3. The material models used for the constituents: T800S Fiber and F3900 Matrix, the characterization of the experimental data used in material models and calibration of certain material properties are discussed in detail in Chapter 4. In Chapter 5, the virtual test specimens including the geometry of the specimens, finite element analysis details including boundary conditions, and the results pertaining to each of the five in-plane tests are discussed. Finally, in Chapter 6, the thesis work and findings are summarized.

# CHAPTER 2

# OVERVIEW OF MAT_213

An orthotropic elasto-plastic material model implemented as MAT_213 in LS-DYNA is a generalized model suitable for any composite architecture with homogenized properties. The material model has three sub-models: deformation, damage and failure, each driven by its own set of tabulated input. The deformation model predicts the linear and the non-linear behavior of the composite [3].

## 2.1 MAT_213 Constitutive Model Overview

The generalized Hooke's Law for a 3D orthotropic material is given by

$$\sigma_{ij} = C_{ijkl}\varepsilon_{kl} \tag{2.1}$$

where

$$C = S^{-1} = \begin{bmatrix} \frac{1}{E_{11}^{T/C}} & -\frac{\nu_{21}}{E_{22}^{T/C}} & -\frac{\nu_{31}}{E_{33}^{T/C}} & 0 & 0 & 0 \\ & \frac{1}{E_{22}^{T/C}} & -\frac{\nu_{32}}{E_{33}^{T/C}} & 0 & 0 & 0 \\ & & \frac{1}{E_{33}^{T/C}} & 0 & 0 & 0 \\ & & & \frac{1}{G_{12}} & 0 & 0 \\ & Sym & & & \frac{1}{G_{23}} & 0 \\ & & & & & \frac{1}{G_{31}} \end{bmatrix}^{-1} \tag{2.2}$$

The superscript in $E_{ii}^{T/C}$ in Eqn. (2.2) represents the tension or compression modulus respectively. If the strains are negative, the corresponding modulus in the stiffness matrix is the compressive modulus. If the strains are greater than zero, the corresponding modulus in the stiffness matrix is the tension modulus.

The plasticity algorithm of the material model is driven by the tabulated experimental data consisting of one or more sets of 12 stress-strain curves at a specific temperature and strain-rate combination. The 12 stress-strain curves can be obtained through physical [4] or virtual testing [13] of the composite -1,2 and 3 direction tension, 1,2 and 3 direction compression, 12, 23 and 31 plane shear, 12, 21 and 31 plane 45° off-axis tension or compression tests.

The yielding of the material is determined by a general orthotropic three-dimensional yield function based on Tsai-Wu failure model and is given as

$$f(\sigma) = -1 + \begin{pmatrix} F_1 & F_2 & F_3 & 0 & 0 & 0 \end{pmatrix} \begin{bmatrix} \sigma_{11} \\ \sigma_{22} \\ \sigma_{33} \\ \sigma_{12} \\ \sigma_{23} \\ \sigma_{31} \end{bmatrix} + \begin{bmatrix} \sigma_{11} \\ \sigma_{22} \\ \sigma_{33} \\ \sigma_{12} \\ \sigma_{23} \\ \sigma_{31} \end{bmatrix}^T \begin{bmatrix} F_{11} & F_{12} & F_{13} & 0 & 0 & 0 \\ F_{12} & F_{22} & F_{23} & 0 & 0 & 0 \\ F_{13} & F_{23} & F_{33} & 0 & 0 & 0 \\ 0 & 0 & 0 & F_{44} & 0 & 0 \\ 0 & 0 & 0 & 0 & F_{55} & 0 \\ 0 & 0 & 0 & 0 & 0 & F_{66} \end{bmatrix} \begin{bmatrix} \sigma_{11} \\ \sigma_{22} \\ \sigma_{33} \\ \sigma_{12} \\ \sigma_{23} \\ \sigma_{31} \end{bmatrix} \tag{2.3}$$

where

$$F_1 = \frac{1}{\sigma_{11}^T} - \frac{1}{\sigma_{11}^C} \quad F_{11} = \frac{1}{\sigma_{11}^T \sigma_{11}^C} \qquad F_{44} = \frac{1}{\sigma_{12}^2} \tag{2.4}$$

$$F_2 = \frac{1}{\sigma_{22}^T} - \frac{1}{\sigma_{22}^C} \; F_{22} = \frac{1}{\sigma_{22}^T \sigma_{22}^C} \quad F_{55} = \frac{1}{\sigma_{23}^2} \tag{2.5}$$

$$F_3 = \frac{1}{\sigma_{33}^T} - \frac{1}{\sigma_{33}^C} \; F_{33} = \frac{1}{\sigma_{33}^T \sigma_{33}^C} \quad F_{66} = \frac{1}{\sigma_{31}^2} \tag{2.6}$$

and the off-diagonal yield function coefficients are defined as

$$F_{ij} = \frac{2}{\left(\sigma_{45}^{i-j}\right)^2} - \frac{F_i + F_j}{\sigma_{45}^{i-j}} - \frac{1}{2}(F_{ii} + F_{jj} + F_{kk}) \quad i, j = 1,2,3, k = i + 3 \tag{2.7}$$

The evolution of the yield function coefficients is a function of the effective plastic strain denoted as $\lambda$, determined by the set of twelve input stress-strain curves at various temperatures and strain rates. The evolution of the components of the plastic strains are computed using non-associative flow rule that relates the plastic strain components to the effective plastic strain as

$$\dot{\boldsymbol{\varepsilon}}_p = \dot{\lambda} \frac{\partial h}{\partial \boldsymbol{\sigma}} \tag{2.8}$$

The plastic potential function, $h$, is expressed as

$$h = \sqrt{H_{11}\sigma_{11}^2 + H_{22}\sigma_{22}^2 + H_{33}\sigma_{33}^2 + 2H_{12}\sigma_{11}\sigma_{22} + 2H_{23}\sigma_{22}\sigma_{33} + 2H_{31}\sigma_{33}\sigma_{11} + H_{44}\sigma_{12}^2 + H_{55}\sigma_{23}^2 + H_{66}\sigma_{31}^2} \tag{2.9}$$

where $H_{ii}$ are the flow rule coefficients specified by the user. A purely elastic behavior analysis can be carried out by assigning a zero value to the flow rule coefficients. For example, if a material exhibits elastic behavior with tension-compression asymmetry and brittle failure in a particular principal direction, the plasticity algorithm can be skipped,

thereby significantly reducing the computational time. The additional details of the deformation, damage and failure sub-models can be found in prior research [2]–[5].

## 2.2 MAT_213 Failure Models

Currently there are four failure criteria in MAT_213 – the Principal Strain Failure Criterion (PSFC), Tsai-Wu Failure Criterion (TWFC), Puck Failure Criterion (PFC) and Generalized Tabulated Failure Criterion (GTFC).

In PSFC, the material failure is initiated when strain in any of the principal material directions reach the ultimate failure strain ($\varepsilon_u$) in that direction

$$\frac{\varepsilon_{ii}}{(\varepsilon_u)_{ii}} - 1 \geq 0 \qquad i = 1,2,3 \tag{2.10}$$

$$(\varepsilon_u)_{ii} = \begin{cases} (\varepsilon_u^t)_{ii} & if \quad \varepsilon_{ii} \geq 0 \\ (\varepsilon_u^c)_{ii} & if \quad \varepsilon_{ii} < 0 \end{cases} \tag{2.11}$$

$$\frac{|\varepsilon_{ij}|}{(\varepsilon_u)_{ij}} - 1 \geq 0 \qquad ij = 12,23,13 \tag{2.12}$$

In TWFC, the material failure occurs when $f(\sigma) \geq 0$ in Eqn. (2.3). The coefficients for TWFC in Eqn. (2.4), Eqn. (2.5), Eqn. (2.6) and Eqn. (2.7) are constants and use failure stresses in each respective direction rather than evolving yield stresses when assessing failure. The Puck's failure criterion is based on the analysis of action plane model for transversely isotropic unidirectional fiber-reinforced composite lamina. In the case of pure normal stress (tension or compression), the plane on which it is acting is the action plane. The fracture plane is the plane where fracture initiates. Failure initiation is detected by computing the

stress values acting on the fracture plane. PFC implementation details in MAT_213 can be found in [5].

The GTFC model can be used when the failure surface of a composite is an arbitrary shaped surface that cannot be defined by smooth mathematical function of stresses (or strains) as shown in Figure 2.1. Instead, a user-defined failure surface is used. The stress and strain invariants use the cylindrical co-ordinate system for defining points on the failure surface. The failure surface in stress/strain space is converted to invariant $r-\theta$ space. The location and magnitude of the point in the failure surface is determined by two independent variables and one dependent variable, respectively. The two independent variables are $\theta_{IP}$ and $\sigma_{11}$ for the case of in-plane state of stress. Similarly, for the out-of-plane state of stress, the independent variables are $\theta_{OOP}$ and $\sigma_{33}$. The $\theta$ in $r-\theta$ space is computed for in-plane state of stress as follows

$$\theta_{IP} = \cos^{-1}\left(\frac{\sigma_{22}}{\sqrt{\sigma_{22}^2+\sigma_{12}^2}}\right) \text{ if } \sigma_{12} > 0$$

$$\theta_{IP} = -\cos^{-1}\left(\frac{\sigma_{22}}{\sqrt{\sigma_{22}^2+\sigma_{12}^2}}\right) \text{ if } \sigma_{12} < 0 \qquad (2.13)$$

If $\sigma_{12} > 0$, then $0 \le \theta_{IP} \le 180^\circ$ and if $\sigma_{12} < 0$ then $0 \le \theta_{IP} \le -180^\circ$, thereby constraining $\theta_{IP}$ to lie between-$180^0$ to $180^0$. Similarly, $\theta$ in using out-of-plane state of stress is computed as

$$\theta_{OOP} = \cos^{-1}\left(\frac{\sigma_{13}}{\sqrt{\sigma_{13}^2 + \sigma_{23}^2}}\right) \text{ if } \sigma_{23} > 0$$

$$\theta_{OOP} = -\cos^{-1}\left(\frac{\sigma_{13}}{\sqrt{\sigma_{13}^2 + \sigma_{23}^2}}\right) \text{ if } \sigma_{23} < 0 \tag{2.14}$$

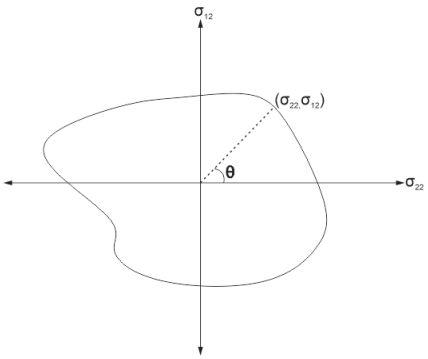


Figure 2.1: Schematic Representation of Failure Surface in In-plane Stress State

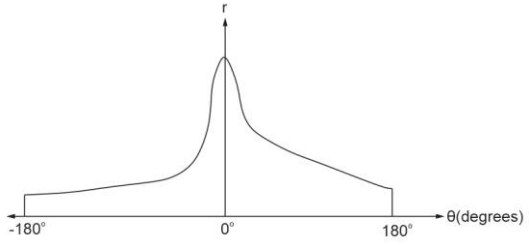


Figure 2.2: Schematic Representation of the Failure Surface in $r-\theta$ Space

If $\sigma_{23} > 0$, then $0 \le \theta_{OOP} \le 180^\circ$ and if $\sigma_{23} < 0$ then, $0 \le \theta_{OOP} \le -180^\circ$. Figure 2.1 shows the graphical representation of the relation between stresses and $\theta$ for an in-plane stress state.

The value of $r$ in $r-\theta$ space defines the magnitude of the failure strain for a given value of $\theta$. The values of $r$ for the in-plane state of stress, $r_{IP}$, and the out-of-plane state of stress, $r_{OOP}$, are computed in terms of strain as

$$r_{IP,F} = \sqrt{\varepsilon_{11}^2 + \varepsilon_{22}^2 + 2\varepsilon_{12}^2} \tag{2.15}$$

$$r_{OOP,F} = \sqrt{\varepsilon_{33}^2 + 2\varepsilon_{13}^2 + 2\varepsilon_{23}^2} \tag{2.16}$$

Figure 2.2 shows a schematic of the user input of $r-\theta$ curve for an arbitrary in-plane or out-of-plane stress state. The failure variables for in-plane state of stress and the out-of-plane state

of stress are the equivalent strain, $r_{IP}$ and $r_{OOP}$, respectively. Both, $r_{IP}$ and $r_{OOP}$ are computed independently using Eqn. (2.15) and Eqn. (2.16). The corresponding $\theta_{IP}$ and $\theta_{OOP}$ are computed using Eqn. (2.13) and Eqn. (2.14) using element stresses at the current timestep. The equivalent strain at failure for in-plane, $r_{IP,F}$ and out-of-plane, $r_{OOP,F}$ state of stress corresponding to $\theta_{IP}$ and $\theta_{OOP}$ at the current time step is obtained via table lookup from the user-defined $r-\theta$ tabular data. The in-plane and out-of-plane erosion values are computed at the current time step as shown in Eqn. (2.17) and Eq. (2.18). The interaction between in-plane and out-of-plane erosion is considered using Eqn. (2.19), where *n* is any arbitrary number greater than zero, specified by the user.

$$d_{IP} = \frac{r_{IP}}{r_{IP,F}} \tag{2.17}$$

$$d_{OOP} = \frac{r_{OOP}}{r_{OOP,F}} \tag{2.18}$$

$$d = \sqrt[n]{d_{IP}^{n} + d_{OOP}^{n}} \tag{2.19}$$

The element is marked for erosion if $d$ in Eqn. (2.19) is equal to or greater than 1. If *n* is equal to zero, then the element is marked for erosion if either $d_{IP}$ or $d_{OOP}$ is equal to or greater than 1.

# CHAPTER 3

# VIRTUAL TESTING SOFTWARE SYSTEM

Virtual Testing Software System (VTSS) [13] is used for generating the virtual test specimens for finite element analysis and for subsequent, post-processing of finite element results. VTSS capabilities include generating the specimen geometry and finite element mesh for 1-direction tension, 1-direction compression, 2-direction tension, 2-direction compression, 1-2 plane shear, 2-3 plane shear, 1-2 plane off-axis and 2-3 plane off-axis tests along with appropriate boundary conditions, and post-processing to obtain the homogenized response of the composite. Currently, VTSS generates one or more RUCs for unidirectional composites by defining the FE model in terms of fiber and matrix phases.

The basic building block for the virtual specimens is a unit cell. The unit cell is assumed to be a square packed cell and is extruded in the fiber direction to generate solid finite elements. On the left in Figure 3.1 is an optical microscope image of the T800-F3900 unidirectional composite that is approximated in finite element analysis through the use of repeating RUCs, a typical one being shown on the right side.

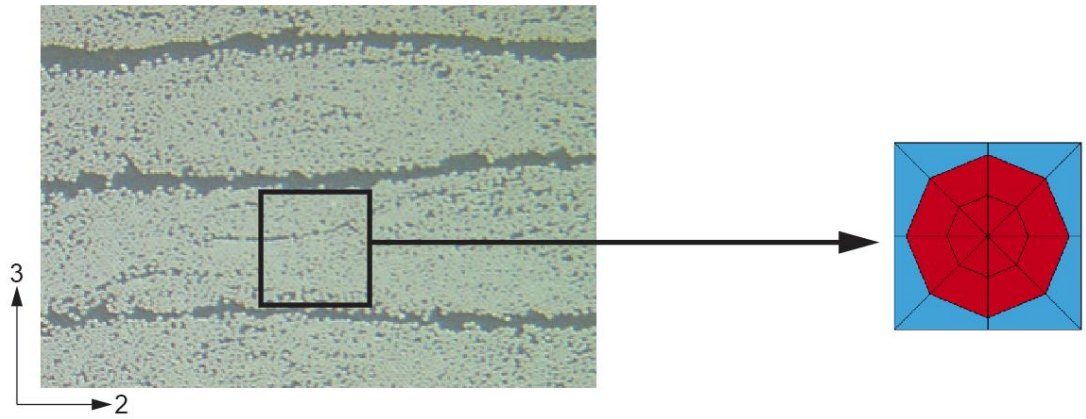


Figure 3.1: (Left) Optical Microscope Image of the T800-F3900 Composite (Right) One RUC showing the Fiber (red) and the Matrix (blue)

The unit cell is generated by specifying the geometric parameters related to its geometry as shown in Figure 3.2 – size of the unit cell – *a*, radius of the unit cell – *r*, angle of the radial line - $\alpha$ , element length along the radial line – *dxy*, element length along the depth of the unit cell – *dz*, and length of the unit cell along the fiber longitudinal direction – *L*.

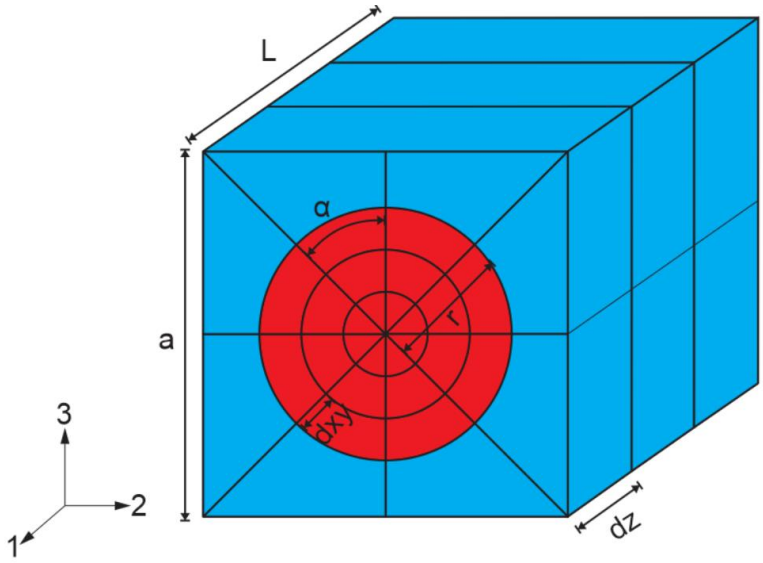


Figure 3.2: Unit Cell Geometric Parameters

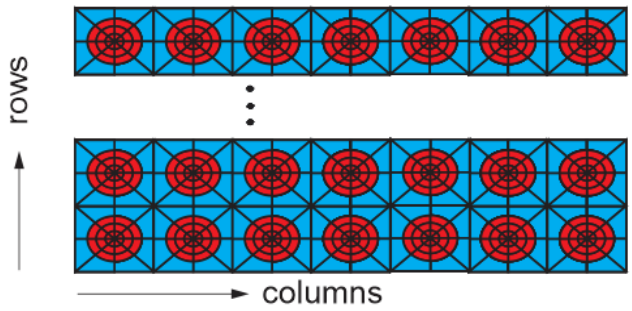


Figure 3.3: Typical Stack of Unit Cells

The virtual specimen geometry is generated by replicating the unit cell in an array of rows and columns. The number of columns and number of rows are based on the dimensions of the virtual test specimen as shown in Figure 3.3.

The fiber phase has two types of elements. The fiber elements at the center of the unit cell are 6-noded wedge elements. The fiber elements other than those at the center of the unit cell are 8-noded hexahedral elements. The matrix phase elements are 8-noded hexahedral elements. In addition to generating the unit cell, the geometric parameters can also be used for controlling the mesh shape and mesh size. Mesh shape can be controlled through angle $\alpha$. The permissible angles in VTSS are 9°, 15°, 22.5° and 45°. The changes in shape of the mesh for constant *dxy* and *dz* with respect to the change in $\alpha$ are shown in Figure 3.4.

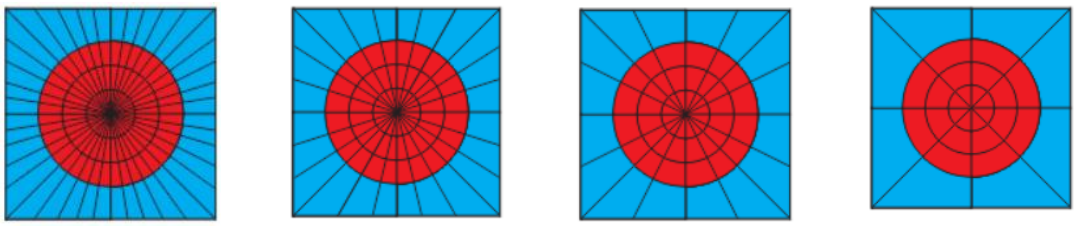

(a) (b) (c) (d)

Figure 3.4: Mesh Shape for Different $\alpha$ (a) $\alpha = 9^{\circ}$ (b) $\alpha = 15^{\circ}$ (c) $\alpha = 22.5^{\circ}$ (d) $\alpha = 45^{\circ}$

For every angle $\alpha$, the mesh size can be varied through *dxy* and *dz*. *dxy* can be chosen as a factor of the fiber radius and *dz* as a factor of the unit cell length. The change in mesh size by reducing *dxy* and *dz* by a factor of 2 is shown in Figure 3.5.

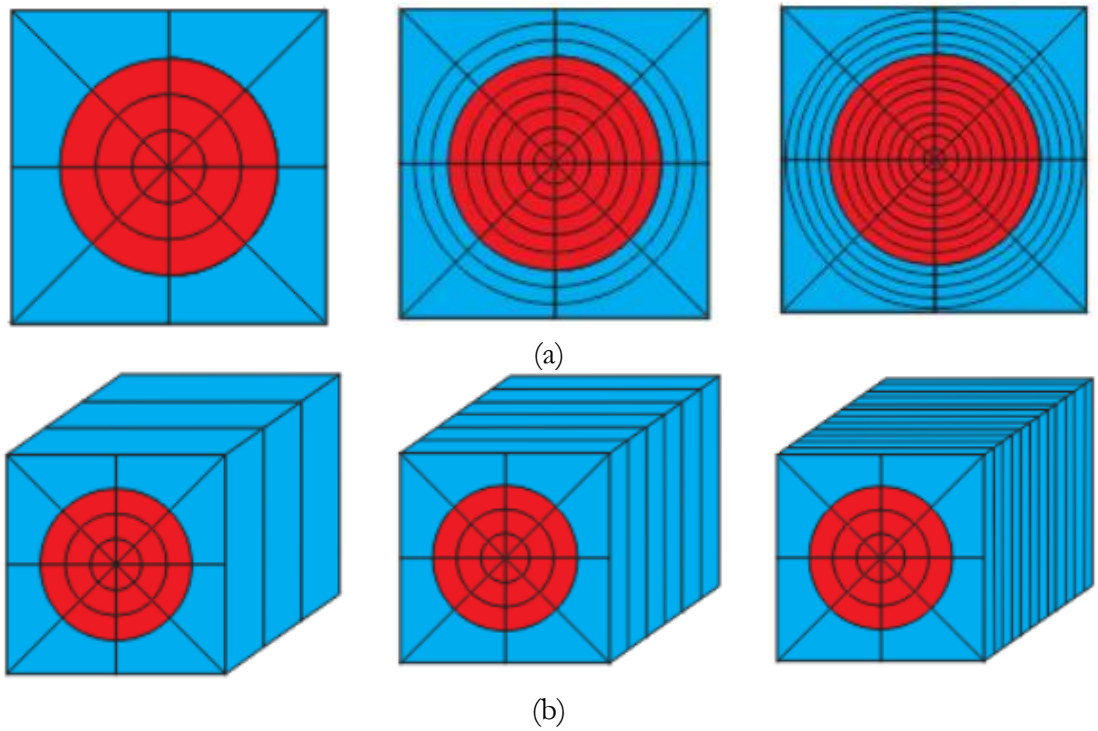

(a)

(b)

Figure 3.5: Mesh Size at $\alpha = 45^{\circ}$ for different (a) *dxy* and (b) *dz*

Complete control over the mesh shape and mesh size can be obtained through different combination of $\alpha$, *dxy* and *dz*. The desirable aspect ratio (AR) close to 1 can be achieved for the fiber and the matrix elements.

A virtual gage section can be defined for the specimen geometry that is away from the boundary and in the vicinity of the center of the virtual specimen as illustrated by yellow colored region in Figure 3.6. The width of the gage section can be varied by specifying the gage section region as *maximum* or *minimum* in VTSS. The gage section width is equal to the

specimen width and the gage section thickness is equal to the specimen thickness with the specification as *maximum*. The gage section width and thickness are equal to size of the unit cell a with the *minimum* specification. The length of the gage section along the fiber direction for both specifications is equal to $dz$.

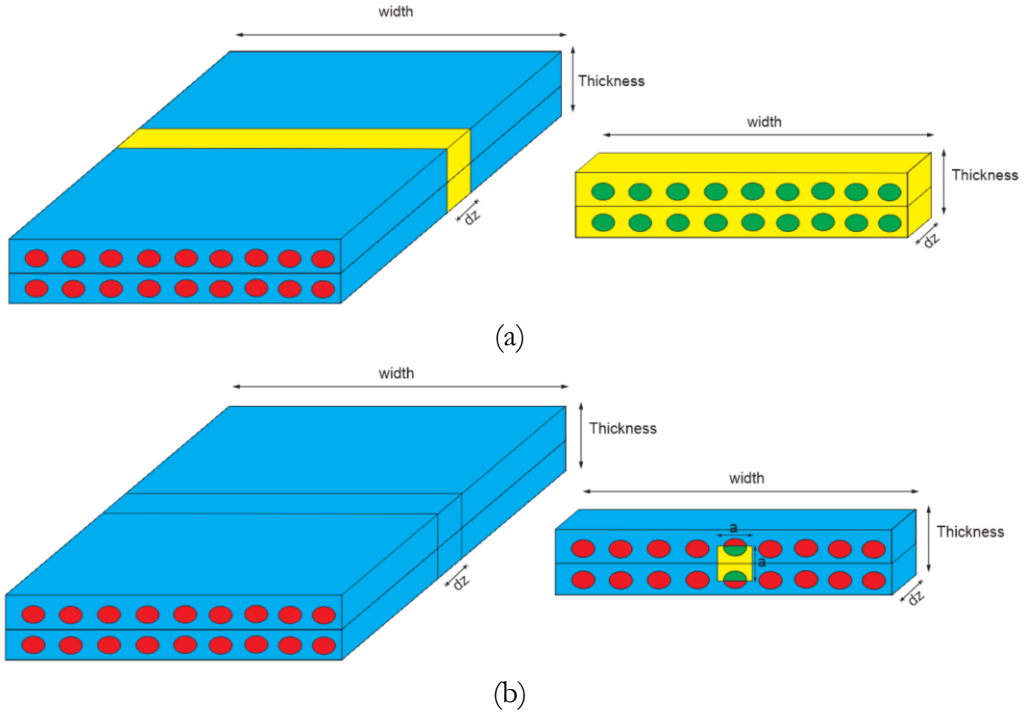


Figure 3.6: Typical Gage Section Region (a) Maximum (b) Minimum

After the finite element analysis, the homogenized response of the composite is obtained using a simple volumetric averaging of the stresses and the strains of the fiber and matrix elements in the gage section as

$$\bar{P}_h = \frac{\sum_{j=1}^{e_t} \left( \frac{\sum_{i=1}^{n_{e_t}} \bar{P}_i V_i}{\sum_{i=1}^{n_{e_t}} V_i} \right)_j V_j}{\sum_{j=1}^{e_t} V_j} \tag{3.1}$$

where

$\bar{P}_h$ is the homogenized material property (stress or strain) at a given time step

$e_t$ is the number of different element types

$n_{e_t}$ is the number of elements in the j$^{th}$ element type

$\bar{P}_i$ is the material property of the i$^{th}$ element. Material property is the average of properties at all integration points

$V_i$ is the volume of the i$^{th}$ element

# CHAPTER 4

# MATERIAL MODEL DESCRIPTION AND MATERIAL CHARACTERIZATION

In this chapter characterization of the T800S carbon fiber is discussed first followed by the characterization of F3900 epoxy resin. When the relevant experimental data is unavailable, the properties of the constituents are derived through virtual testing of the composite. The properties of the constituents are computed in such a way that the homogenized response of the composite virtual test is consistent with the *Model Curve* of the composite. A *Model Curve* is a representative stress strain curve obtained from the average response computed from a minimum of three replicates of the QS-RT experiments [4]. The model stresses for each test are computed by least-square fit of the stresses obtained from three or more replicates at each experimental strain value. In the rest of the thesis, the *Model Curve* (of the composite) is represented by a red colored solid line in the graphs, the T800S fiber by blue solid and dashed lines, and the F3900 by purple colored solid lines, and the input curves used in the material model are marked by orange solid lines.

## 4.1 T800S Carbon Fiber Characterization

T800S is an intermediate modulus and high strength carbon fiber that is assumed to be linear elastic and transversely isotropic. The longitudinal tensile strength and the longitudinal modulus of the fiber are obtained from Toray Composite Materials America (Toray CMA)[14] and calibrated to correlate with virtual testing results. The transverse modulus, longitudinal Poisson's ratio and transverse Poisson's ratio were obtained from the

inverse analysis of composite that was similar to the T800/F3900 composite and from the carbon fibers similar to T800S [13]. The shear modulus was obtained by inverse analysis using MAC/GMC, which is a Micromechanics Analysis Code based on Generalized Method of Cells [20]. In inverse analysis, the constituent properties in MAC/GMC for the fibers are optimized to match the experimental results of T800/F3900 available from Wichita State University [15] using a least square error fit.

MAT_213 is used for modeling the carbon fiber. As discussed in Chapter 2, only the elastic behavior of the material is considered in this research by specifying the plastic potential function coefficients as zero (see Eqn. (2.9)). In addition, it should be noted that MAT_213 is perhaps the only material model in LS-DYNA with the capacity to distinguish between tension and compression asymmetric behavior in an orthotropic material.

Initially the longitudinal compression modulus of T800S was considered to be the same as longitudinal tension modulus. The 1-direction compression (the finite element model used is discussed in Section 5.3.3) response of the composite was significantly stiffer compared to the *Model Curve* (see Figure 4.1). When longitudinal compression modulus of the carbon fiber was reduced to half the longitudinal tension modulus, the 1-direction compression response of the composite was softer compared to the *Model Curve*. By bounding the longitudinal compression modulus between $2(10^7)$ psi and $4(10^7)$ psi, the calibrated longitudinal compression modulus was determined using linear interpolation at the end of the linear regime of the *Model Curve* (approximately at a strain of 0.003). The resulting value of $3.1(10^7)$ psi provided a good match with the *Model Curve* (see Fig. 4.1). During the calibration process, all the other fiber properties were held constant.

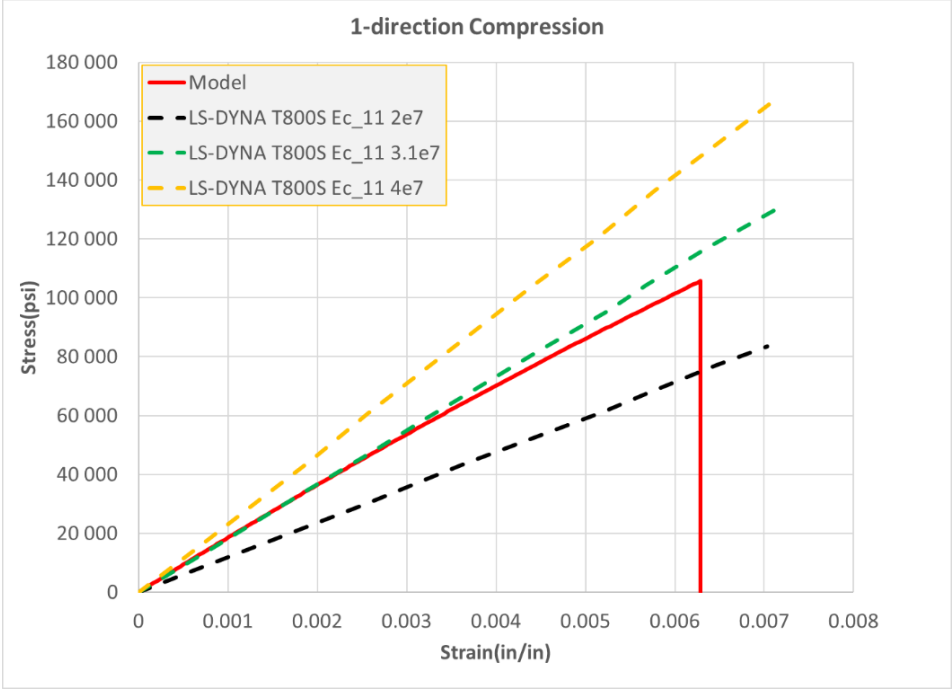


Figure 4.1: Longitudinal Compression Modulus of Fiber

The properties of the carbon fiber used in virtual tests are listed in Table 4.1. The experimental curves in various directions for the T800S fiber are shown in Figs. 4.2, 4.3 and 4.4. It should be noted that there is tension-compression asymmetry in the 1-direction. There is no evidence of a similar asymmetry in the 2 or 3 directions. Finally, in the absence of experimental or inverse analysis data, the 1-2, 2-3 and 1-3 off axis curves are taken to be same as 1-direction tension curves as these properties were found to have little effect on the ultimate composite response. The off-axis curves are only used within MAT_213 to compute the interaction coefficients of the yield function. Since yielding is ignored, the choice of the off-axis data is inconsequential and is only mentioned here for completeness.

Table 4.1: T800S Material Properties

| Engineering Constant | Value |
|---|---|
| $E_{11}$ | $4.0(10^7)\,psi$ |
| $E_{22} = E_{33}$ | $2.25(10^6)\,psi$ |
| $\nu_{31} = \nu_{21}$ | 0.01125 |
| $\nu_{23}$ | 0.25 |
| $G_{12} = G_{13}$ | $1.5(10^7)\,psi$ |
| $G_{23}$ | $1.5(10^7)\,psi$ |

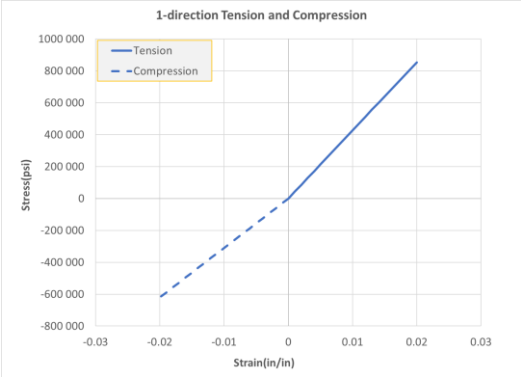


Figure 4.2: 1-direction Tension and Compression Curves for T800S Fiber

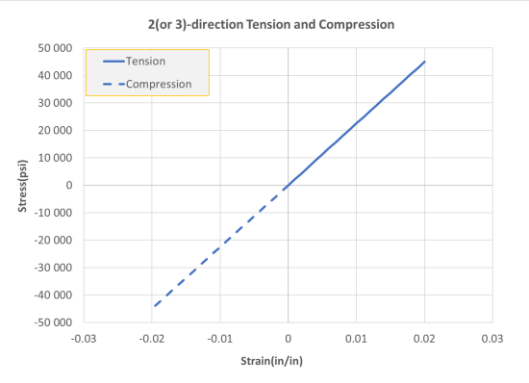


Figure 4.3: 2-direction Tension and Compression Curves for T800S Fiber

The Principal Strain Failure Criterion (PSFC) is used for modeling failure of the fibers. The 1-direction tension failure strain and 1-direction compression failure strain of the T800S are assumed to be the same as T800/F3900 failure strain in 1-direction tension and 1-direction compression [5]. In 2-direction tension, 2-direction compression and 2-1 plane shear, the failure is usually due to the matrix cracking and/or fiber matrix interface debonding and hence in the absence of experimental data, the failure of the fiber is not considered for the

other material directions. The failure strains in other material directions are set to a very large number as shown in Table 4.2 to ensure that the failure does not take place.

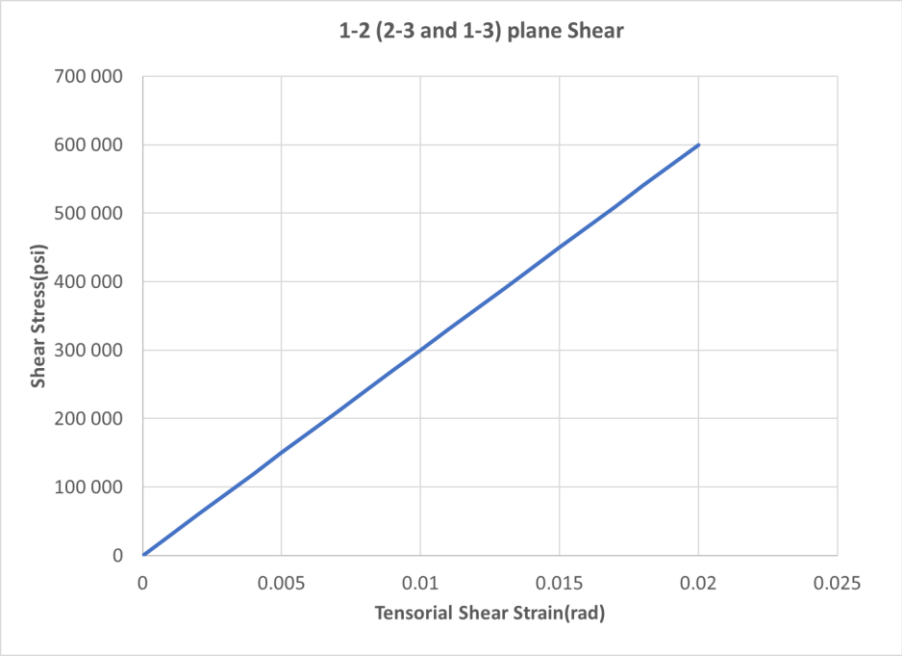


Figure 4.4: 1-2 plane, 2-3 plane and 1-3 plane Shear Curves for T800S Fiber

Table 4.2: Failure Strains for T800S Used in PSFC (MAT_213)

| **Principal material direction** | **Failure strain value** |
|---|---|
| 1-direction Tension | 0.0156 |
| 1-direction Compression | 0.00629 |
| 2-direction Tension / Compression | Does not fail |
| 3-direction Tension / Compression | Does not fail |
| 1-2, 2-3 and 1-3 plane shear | Does not fail |

4.2 F3900 Matrix Characterization

F3900 is a toughened epoxy resin. The experimental response of F3900 in uniaxial tension, uniaxial compression and Iosipescu shear as shown in Figure 4.5 [22], indicates that the yielding behavior of F3900 in uniaxial tension is different from uniaxial compression. In

uniaxial tension, F3900 is brittle whereas in uniaxial compression, the matrix exhibits a strain softening behavior followed by re-stiffening. (Fig. 4.5 (b)).

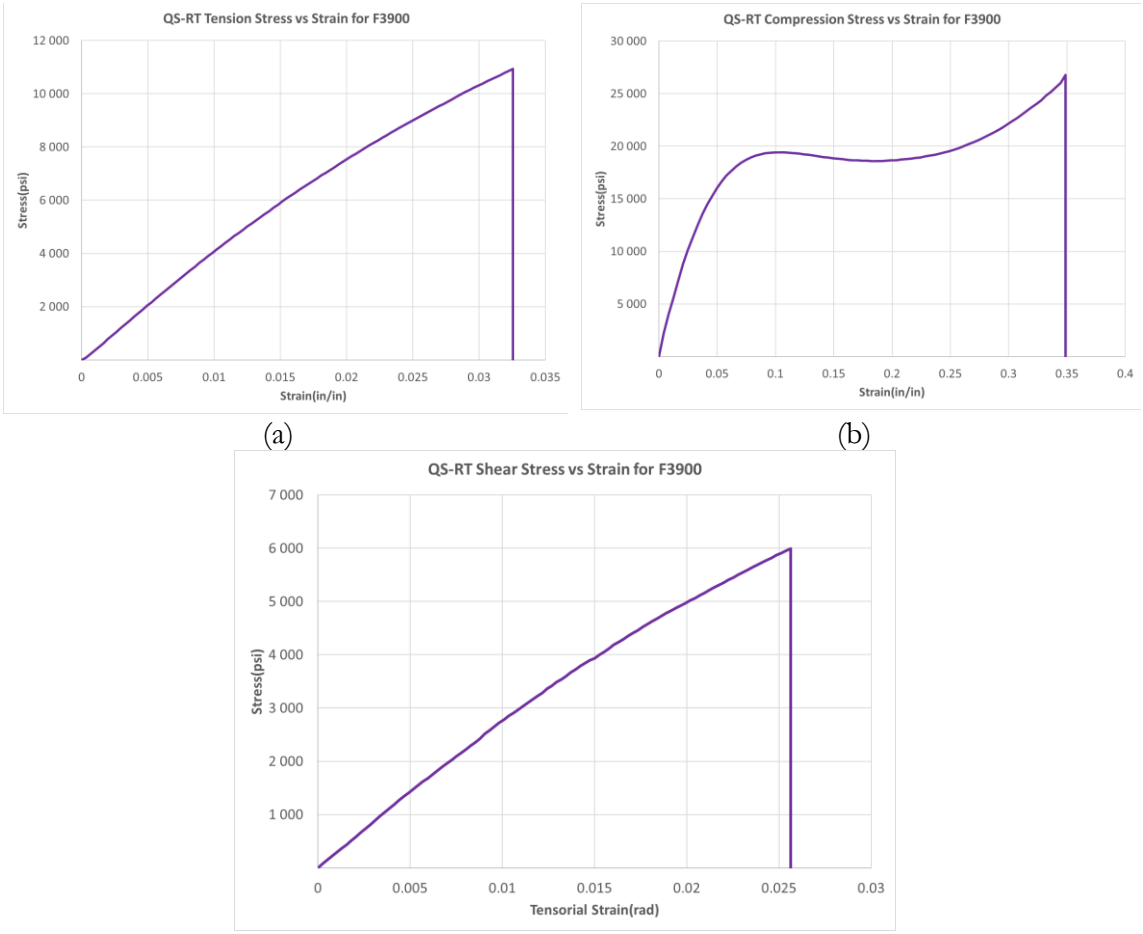


Figure 4.5: F3900 Experimental Response (a) Uniaxial Tension (b) Uniaxial Compression (c) Iosipescu Shear

Different material models as shown in Table 4.3 are used for modeling polymers in LS-DYNA. Amongst all the listed material models, MAT_187 is the only material model which distinguishes between tension and compression behavior of the polymer and allows for the tabulated input for tension, compression and shear behaviors.

Table 4.3: List of Material Models Used for Modeling Polymers in LS-DYNA

| Material Number | Description |
|---|---|
| MAT_03 | Plastic Kinematic/ Isotropic |
| MAT_24 | Piecewise Linear Plasticity (Isotropic) |
| MAT_89 | Plasticity Polymer |
| MAT_141 | Rate Sensitive Polymer |
| MAT_187 | Semi-Analytical Model for Polymers |

Depending on the number of curves used in the input for MAT_187, the yielding of the material can be defined by different types of yield surfaces [18] [23]. The maximum number of load curves which can be input in MAT_187 is four and the minimum number is one. The four load curves are: Plastic Strain vs Yield Stress obtained from uniaxial tension (LCID-T), uniaxial compression (LCID-C), uniaxial shear (LCID-S), and biaxial tension (LCID-B). When only one load curve is used as an input, the yielding of the material is based on von-Mises cylindrical failure surface. When at least two of the four load curves are used as an input, the yielding of the material is based on Drucker-Prager cone, and when at least three of the load curves are used as an input, the yield surface is a modified form of Drucker-Prager cone with $C^1$ continuous yield surface in von-Mises and Pressure space. The multi-element simulation by [22] revealed that the response of F3900 was consistent with the experimental response when all three curves were used: Plastic Strain vs Yield Stress for uniaxial tension (LCID-T), compression (LCID-C) and shear (LCID-S) were used as input along with biaxial tension (LCID-B) curve and an appropriate ratio of biaxial compression to

uniaxial compression (RBCFAC) value. The LCID-T, LCID-C, LCID-S and LCID-B curves used as the input for the F3900 matrix are shown in Figs. 4.6a to 4.6d respectively.

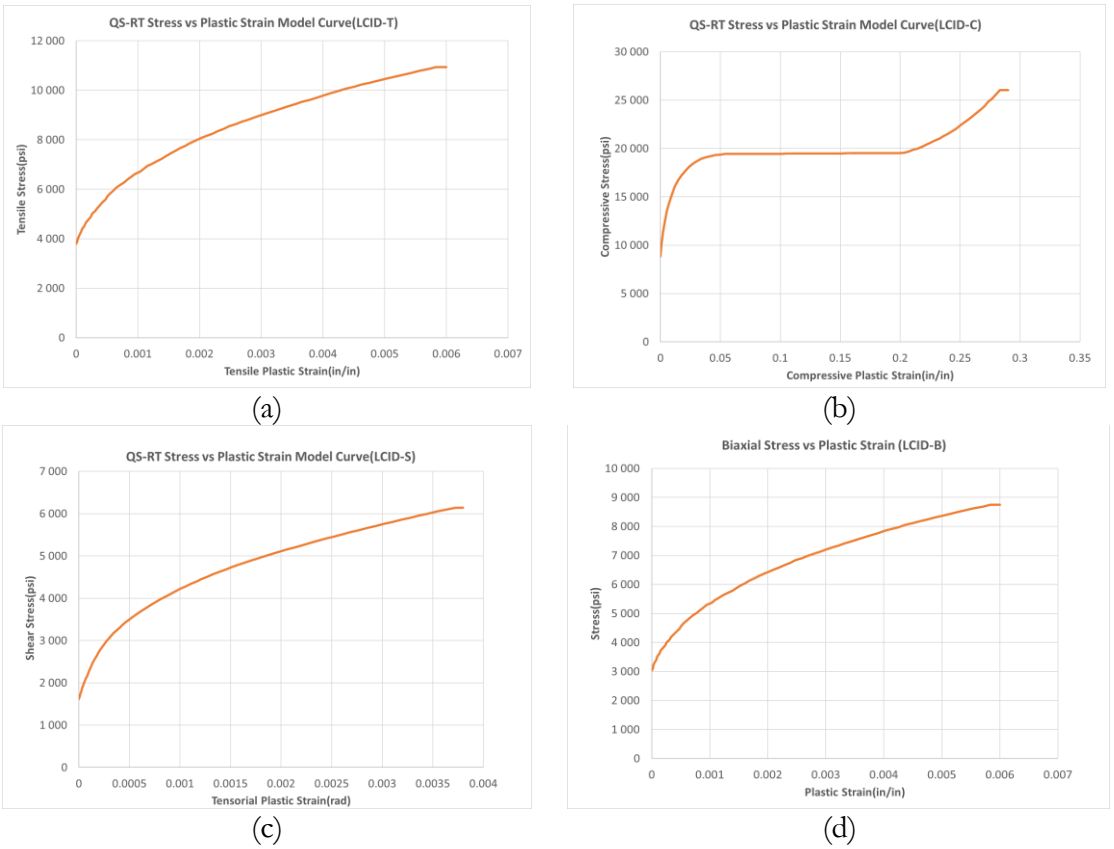


Figure 4.6: MAT_187 Input Curves (a) LCID-T (b) LCID-C(c) LCID-S (d) LCID-B for the F3900 Matrix

Using this combination of the input , the yield surface takes a piecewise linear form [23] as shown in Figure 4.7. The three-dimensional yield surface in stress space is reduced to two-dimensional yield surface in invariant space. Unlike typical von-Mises yield surface, the piecewise linear yield surface shown in Figure 4.7 shows the dependence of von-Mises stress on pressure. The black solid lines in Figure 4.7 are different loading paths and the red solid

line is the yield surface constructed using the von-Mises stress for a pressure value corresponding to that loading direction.

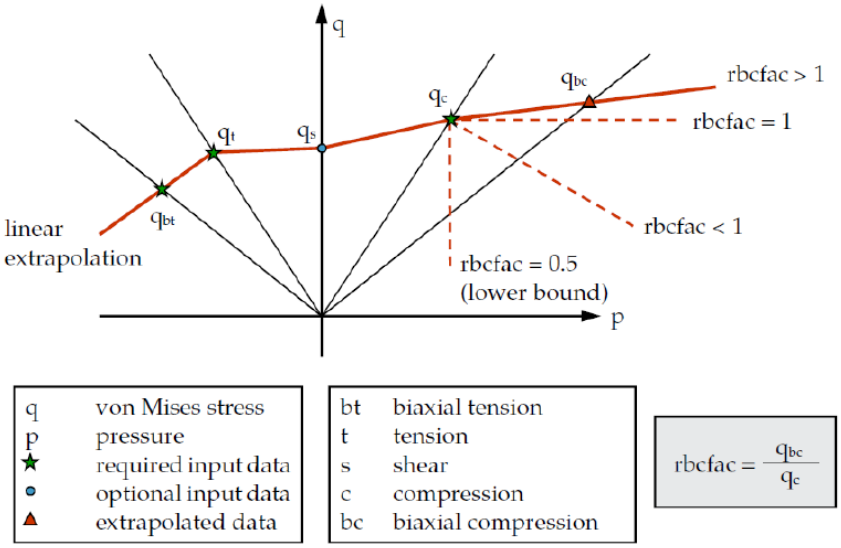

Figure 4.7: Piecewise Linear Yield Surface in MAT_187[23]

The biaxial tension curve was calibrated by scaling the uniaxial tension yield stresses by 80% based on the recommendations from the material model developer [24]. The value of RBCFAC was calibrated by comparing the response of the virtual specimen in 2-direction compression with respect to the *Model Curve* in 2-direction compression. The RBCFAC was varied from 1.5 to 0.833 as shown in Figure 4.8. The response in the linear region was same for all the RBCFAC value however when RBCFAC was 1 and 1.25, there was no non-linearity in the response. The non-linearity in the response of the virtual tests is attributed to the plasticity of the matrix elements. With RBCFAC of 1 and 0.833, the yielding of the matrix elements resulted in the non-linear response of the virtual test specimen. The RBCFAC lower than 1 resulted in the premature yielding of the specimen and greater than 1 resulted in no yielding of the specimen hence the RBCFAC was considered as 1 since the

virtual test response is closest to the *Model Curve*. The matrix properties used for virtual tests are specified in Table 4.5.

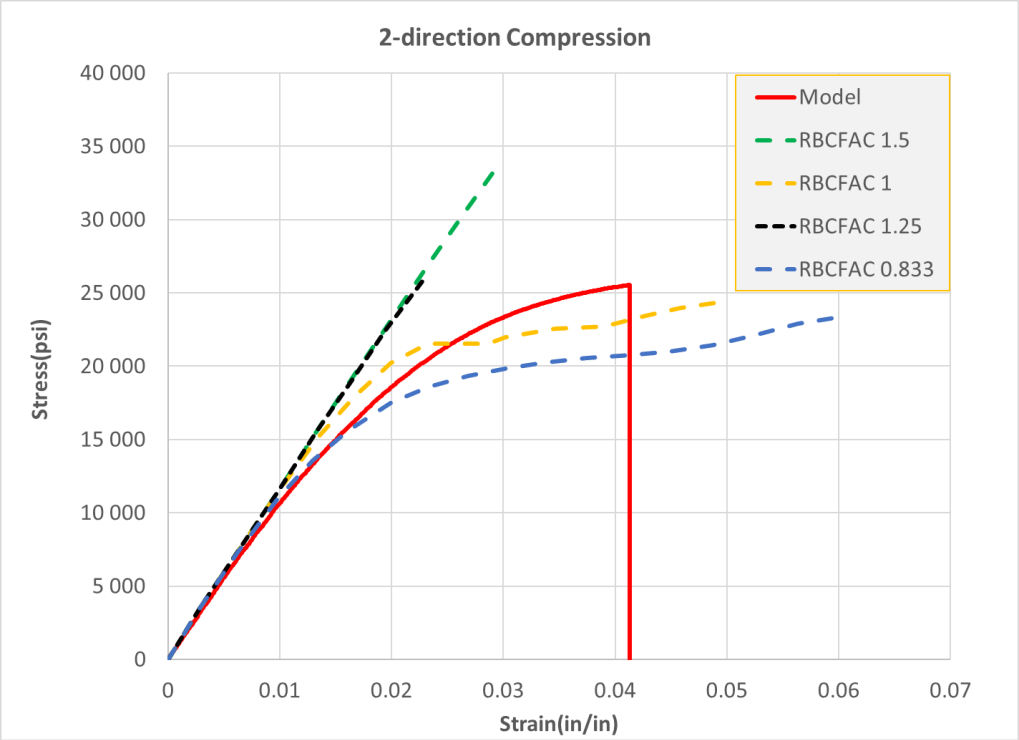


Figure 4.8: Response of Virtual Test Specimen in 2-direction Compression for Different Values of RBCFAC

Table 4.5: F3900 Material Properties

| **Material Constant** | **Value** |
|---|---|
| Bulk Modulus (psi) | 602632 |
| Shear Modulus (psi) | 147503 |
| Elastic Modulus (psi) | 409235 |
| RBCFAC | 1 |
| Elastic Poisson's ratio | 0.387 |
| Plastic Poisson's ratio | 0.386 |

The failure in MAT_187 can be defined in terms of tabulated input. An incremental formulation is used for determining the failure that is based on the damage parameter, $d$, which is a function of equivalent plastic strain, $\varepsilon_p$, equivalent plastic strain at failure obtained from uniaxial tension test, $\varepsilon_{pf}$ and stress triaxiality. The failure of the matrix element occurs when damage parameter equals or is greater than critical damage parameter, $d_c$, as shown in Eqn. (4.3)[24]. The tabulated input is the factor corresponding to a particular triaxial stress state that scales $\varepsilon_{pf}$.

$$d = \int \frac{\varepsilon_{pf}(0) f\left(-\frac{1}{3}\right)}{\varepsilon_{pf}\left(\dot{\varepsilon}_p\right) f\left(\frac{p}{\sigma_{vm}}\right)} d\varepsilon_p \geq \varepsilon_{pf}\left(\dot{\varepsilon}_p\right) f\left(\frac{p}{\sigma_{vm}}\right) = d_c \tag{4.3}$$

where

$d$ is the damage parameter at the current time step and rate

$d_c$ is the critical damage parameter at the current time step and rate

$\varepsilon_{pf}$ is the equivalent failure strain corresponding to the current rate obtained from uniaxial tension

$\dot{\varepsilon}_p$ is the plastic strain rate

$\frac{p}{\sigma_{vm}}$ is the stress triaxiality at the current time step

The initial $\varepsilon_{pf}$ value is considered to be equal to the plastic strain at failure obtained from the uniaxial tension test of F3900. The plastic strains at failure from the uniaxial

compression and Iosipescu shear are listed in Table 4.6. In the absence of the experimental data for triaxiality less than -0.33 and triaxiality greater than 0.33, an approximate failure curve based on the experimental observations of the epoxy resin EPON 826 [26] as shown in Figure 4.9, is used to characterize the failure of F3900. In [25], a cylindrical specimen is subjected to multiaxial state of stress. The failure in combined axial stress and hoop stress in tension is brittle. The failure strains and stresses under combined stress condition in tension is less than the failure strains and stresses under axial tension. This is attributed to the presence of high hydrostatic pressure. Hence, for the triaxiality less than -0.33 for F3900, in the absence of experimental data, the equivalent plastic strain at failure is considered to be constant and is set equal to 0.005829. Under multiaxial compression stress state, the failure of F3900 for triaxiality greater than 0.33, the equivalent plastic strain at failure is considered to be greater than 0.29. A parabolic fit for the triaxiality greater than 0.33 was assumed based on the equivalent plastic strain at failure of the Iosipescu shear and uniaxial compression.

Table 4.6: Equivalent Plastic Strain at Failure

| **Test** | **Equivalent Plastic Strain at Failure** | $f\left(\frac{p}{\sigma_{vm}}\right)$ | $\frac{p}{\sigma_{vm}}$ |
|---|---|---|---|
| Biaxial Tension | 0.005829 | 1 | -0.67 |
| Uniaxial Tension | 0.005829 | 1 | -0.333 |
| Iosipescu Shear | 0.0473 | 8.116 | 0 |
| Uniaxial Compression | 0.29 | 48.55 | 0.333 |
| Biaxial Compression | 0.84 | 144.86 | 0.67 |

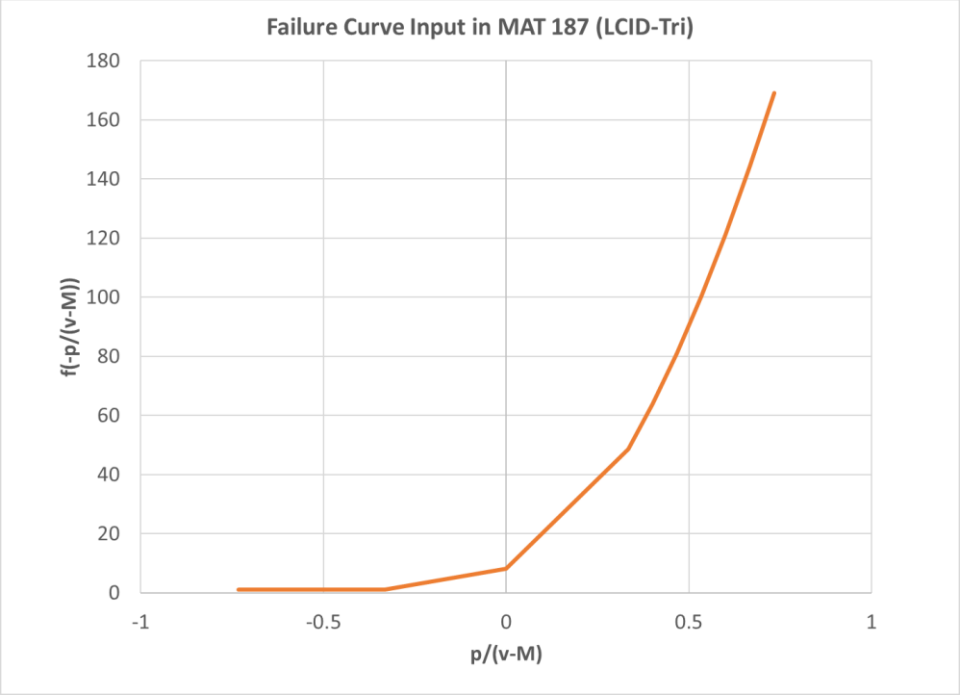

Figure 4.9: Tabulated Failure Curve Input in MAT_187

# CHAPTER 5

## IN-PLANE VIRTUAL TESTS MODEL DESCRIPTION AND RESULTS

The details of the finite element models used for virtual testing are discussed in this chapter along with the results of the five in-plane virtual tests. The virtual test specimens are geometrically equivalent to the experimental specimen geometry. The experimental specimens were machined from different panels [19]. The details of the panel type and number of plies in each panel used for different tests are specified in Table 5.1. The thickness of each ply in PT1 is 0.0076" and the thickness of each ply in PT2 is 0.0077".

Table 5.1: Panel Specifications for Different Tests

| **Test** | **Panel Type** | **Nominal Thickness of the Panel (in)** | **# of plies** |
|---|---|---|---|
| 1-direction Tension | PT1 | 0.122 | 16 |
| 2-direction Tension | PT1 | 0.122 | 16 |
| 1-direction Compression | PT1 | 0.122 | 16 |
| 2-direction Compression | PT1 | 0.122 | 16 |
| 2-1 plane Shear | PT2 | 0.185 | 24 |

The equivalent dimensions of the virtual test specimen were computed by keeping the proportion of $\left[1:\frac{\text{Length}}{\text{Thickness}}:\frac{\text{Width}}{\text{Thickness}}\right]$ of the experimental specimen same for the virtual test specimen for each test. The size of the unit cell is equal to the thickness of the single ply. The thickness of the virtual test specimen is equal to the number of plies used for

the simulation. Preliminary results with different number of plies showed converging trend from 2 plies onwards. Hence, the number of plies for all the verification tests is limited to 2 plies for the computational efficiency. The fiber volume fraction was estimated to be 60% from the optical micrograph image analysis [26].

Three different virtual test models designated as Coarse Model (CM), Medium Model (MM) and Fine Model (FM) were used for convergence analysis for each test with increasing number of nodes and elements going from CM to MM to FM. The aspect ratio for the fiber elements and the matrix elements was reduced from CM to FM. The aspect ratio of the CM, MM and FM for all the five in-plane tests are nearly same for each test. The details of the finite element related parameters like number of nodes, number of elements and aspect ratio used for each model are provided in subsequent sections. An explicit time step integration scheme was used for the virtual tests in LS-DYNA by keeping the kinetic energy minimal in order to replicate a quasi-static test. All the tests were displacement-controlled tests with the displacement rate of 4in/sec and the mass density of F3900 and T800S were scaled up by a factor of 1000 to reduce the computational time.

The in-plane virtual test results with the deformation only are discussed first, followed by results with both deformation and failure.

## 5.1 1-direction Tension

### *Virtual Test Specimen Geometry*

The experimental specimen layout is shown in Figure 5.1, where the shaded region represents the area where fiberglass tabs were used. The gage section has a through thickness

of 0.063" such that $\left(1:\frac{L}{t}:\frac{w}{t}=1:31.65:7.94\right)$. Figure 5.2 shows the virtual test specimen with the equivalent dimensions. The through thickness of the virtual test specimen is computed as 0.01525" such that $\left(1:\frac{L}{t}:\frac{w}{t}=1:32:7.93\right)$. The virtual test specimen does not contain the tabbed sections and the transition zone.

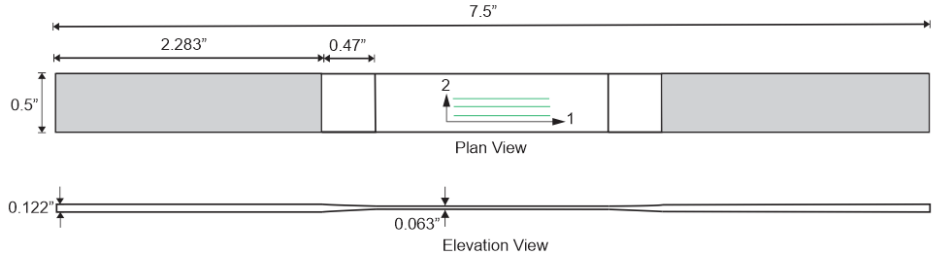


Figure 5.1: 1-direction Tension Experimental Specimen Layout

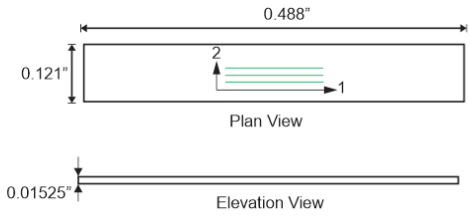


Figure 5.2: 1-direction Tension Virtual Test Specimen Layout

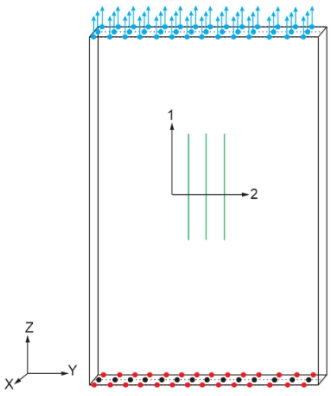


Figure 5.3: Boundary Conditions for 1-direction Tension

*Boundary Conditions and Model Details*

The black colored nodes in Figure 5.3 are restrained in the X, Y and Z directions. The red colored nodes are restrained in the Z direction. The blue colored nodes have displacements applied in the positive Z direction. The VTSS geometric parameter details for

different meshes are provided in Table 5.2. The total number of nodes, elements, maximum and minimum aspect ratio are provided in Table 5.3. Figure 5.4 shows the top view and isometric view of the virtual test specimen.

Table 5.2: VTSS Geometric Parameter Details for 1-direction Tension Test Models

| **Model** | $a$ **(in)** | $r$ **(in)** | $\alpha$ | $dxy$ **(in)** | $dz$ **(in)** | $L$ **(in)** | **# Rows** | **# Columns** |
|---|---|---|---|---|---|---|---|---|
| CM | 0.0076 | 0.00333 | 22.5 | 0.00166 | 0.0024 | 0.488 | 2 | 16 |
| MM | 0.0076 | 0.00333 | 22.5 | 0.00166 | 0.0018 | 0.488 | 2 | 16 |
| FM | 0.0076 | 0.00333 | 22.5 | 0.00166 | 0.0012 | 0.488 | 2 | 16 |

Table 5.3: Model Details for 1-direction Tension Test Models

| **Model** | **# Elements** | **# Nodes** | **Max. AR** | **Min. AR** |
|---|---|---|---|---|
| CM | 313344 | 277365 | 4.985 | 3.011 |
| MM | 417792 | 369369 | 3.740 | 2.758 |
| FM | 625152 | 552024 | 3.29 | 2.56 |

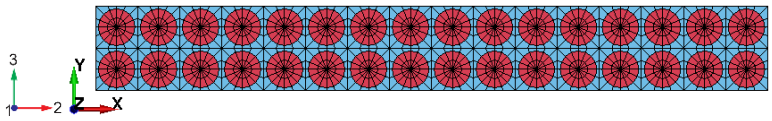


(a)

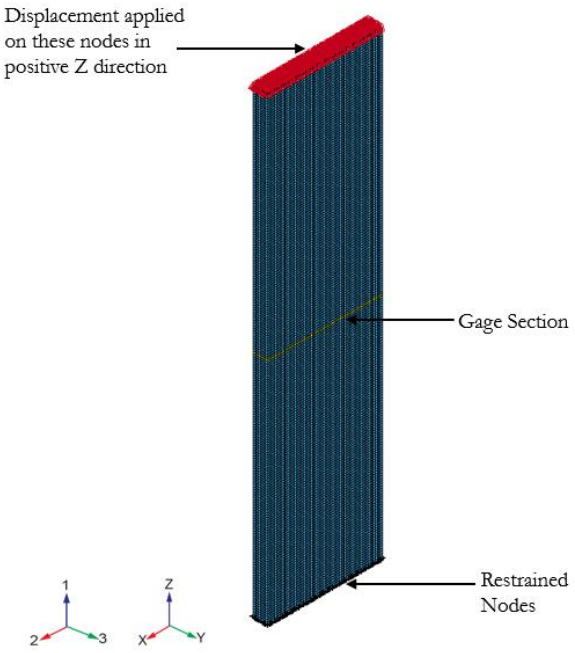


(b)

Figure 5.4: 1-direction Tension Fine Model (a) Top View (b) Isometric View

*Deformation Only 1-direction Tension Test Results*

The 1-direction tension test results for all the three virtual test models (CM, MM and FM) are shown in Figure 5.5. The deformation only response from all the three models is the same. In the *Model Curve*, there is a slight, almost imperceptible concavity with hardening towards the failure strain. The non-linearity in the *Model Curve* could be due to the straightening of the fibers as the experiment progresses [5]. Since the fibers are modeled as straight and without any waviness, the non-linearity observed in the *Model Curve* is not captured in the virtual test. Since failure of the constituents is not considered, the response of the virtual test specimens extends beyond the *Model Curve*. The LS-DYNA plot of the kinetic energy and total energy for FM is shown in Figure 5.6. The total energy and the

internal energy graphs lie on the top of each other. The kinetic energy is negligible compared to the internal energy indicating the inertial effects are negligible in the virtual tests.

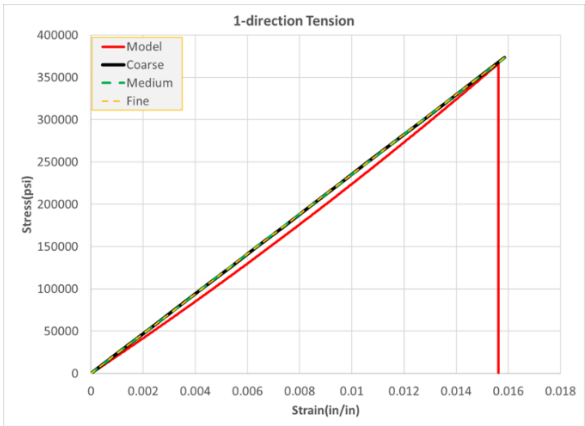


Figure 5.5: Deformation Only 1-direction Tension Response

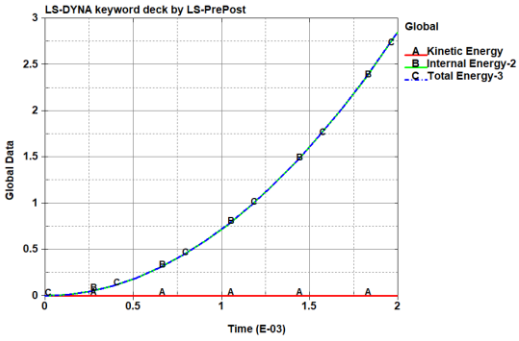


Figure 5.6: LS-DYNA Energy Plots for 1-direction Tension

The contour plot of Z stresses, where Z is the loading direction, in the fiber and the matrix of the gage section for the FM corresponding to the homogenized composite Z stress of 351255 psi from Figure 5.5, is shown in Figure 5.7a. The Z stresses in the fiber elements and the matrix elements are uniform throughout the width of the gage section with the stresses in the fiber elements higher by an order of magnitude of 2 compared to the stresses in the matrix elements. The contour plot of Z strains in the gage section is shown in Figure 5.7b. The Z strains in fiber and matrix elements are same and uniform throughout the width of the gage section.

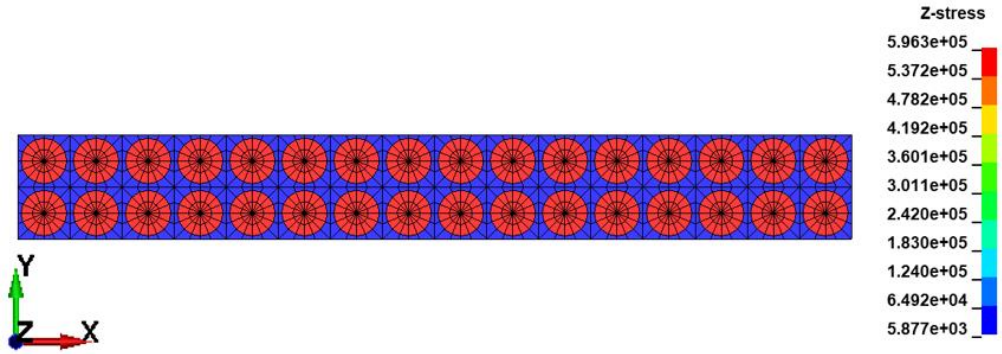


(a)

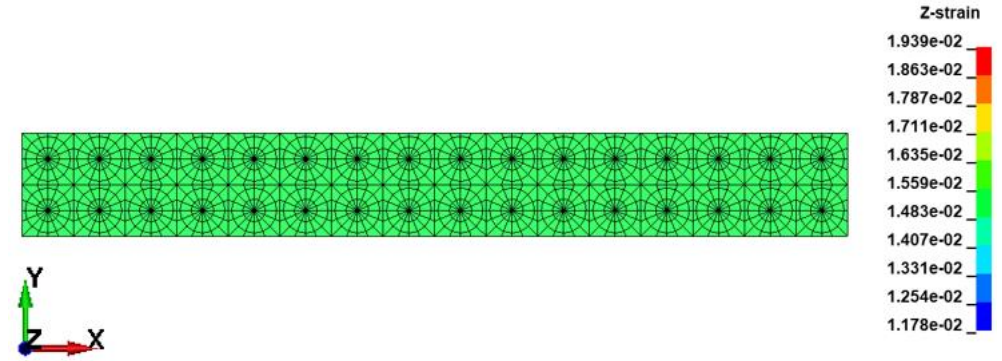


(b)

Figure 5.7: LS-DYNA Contour Plots for 1-direction Tension (a) Z Stress(psi) (b)Z Strain(in/in) in the Gage Section

*Deformation and Failure 1-direction Tension Test Results*

The 1-direction tension results for all the virtual test models (CM, MM and FM) are shown in Figure 5.8a. The failure stress and failure strain from all the three tests were nearly same. Figure 5.8b shows the FM before failure. Three failure zones are highlighted as shown in Figure 5.8c.

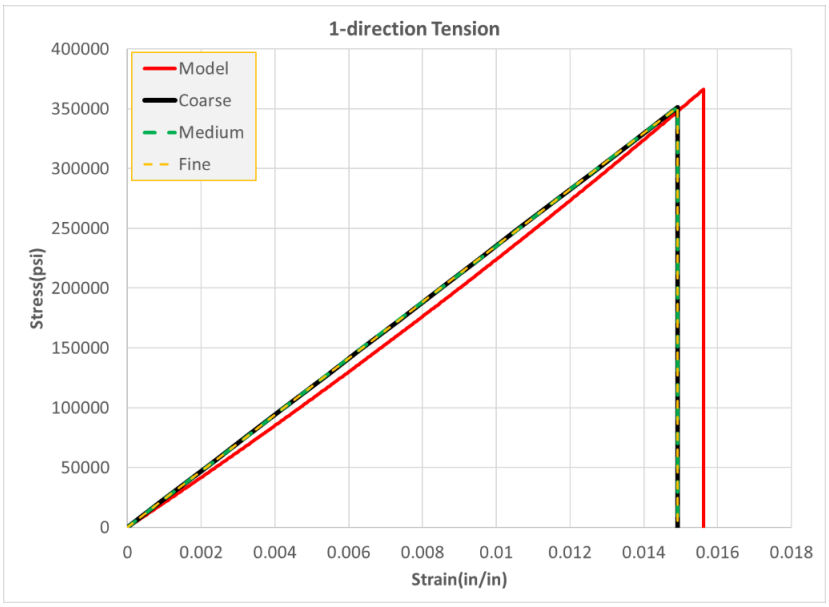


(a)

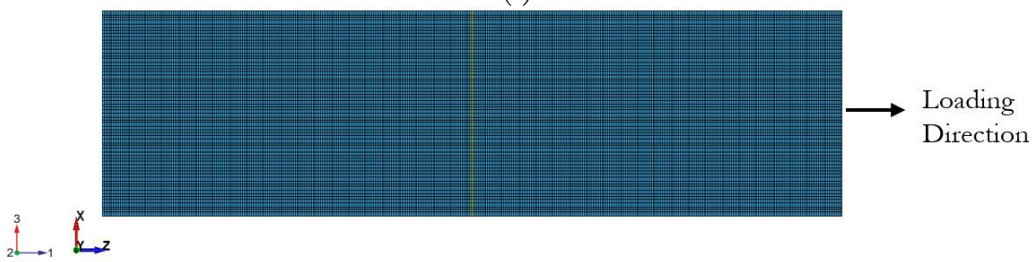


(b)

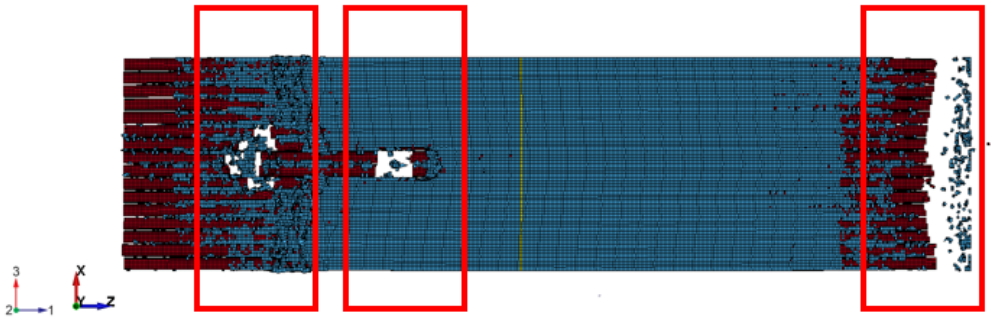

(c)

Figure 5.8: 1-direction Tension (a) Deformation and Failure Response(b) Fine Specimen before Failure (c) Fine Specimen after Failure

Failure initiates in few fiber elements near the fixed boundary and then all the fiber elements near the loading edge fails. The failure pattern in the fibers only is shown in Figure

5.9a. The failure of the fiber in the region away from the edges is uncertain from the d3plots of the simulation. The failure in those regions could be due to the failure of the fibers in compression which could have been resulted from the snapping back of the fibers. The failure pattern in the matrix elements is shown in Figure 5.9b.

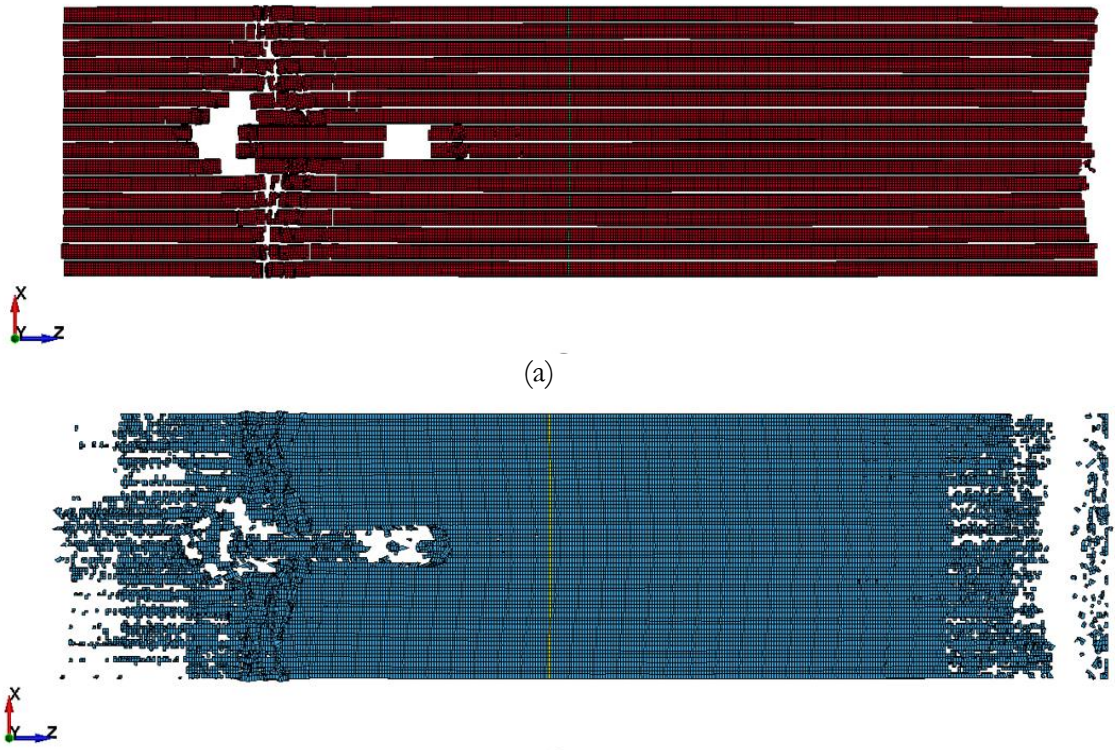


Figure 5.9: 1-direction Tension Failure Pattern (a) Fiber Elements (b) Matrix Elements

## 5.2 2-direction Tension

*Virtual Test Specimen Geometry*

The experimental specimen layout is shown in Figure 5.10, where the shaded region represents the area where fiber glass tabs were used. The experimental specimen is a flat specimen with through thickness of 0.122" such that $\left(1:\frac{L}{t}:\frac{w}{t}=1:18.44:4.1\right)$. Figure 5.11

shows the virtual test specimen with the equivalent dimensions. The through thickness of the virtual test specimen is 0.01525" such that $\left(1:\frac{L}{t}:\frac{w}{t}=1:18.42:4.1\right)$. The virtual test specimen does not contain the tabbed sections and the transition zone.

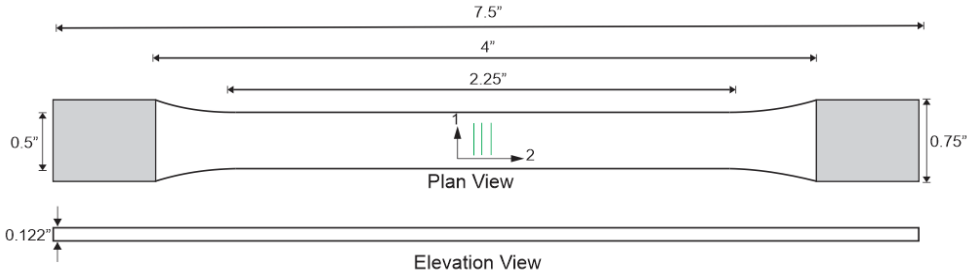


Figure 5.10: 2-direction Tension Experimental Specimen Layout

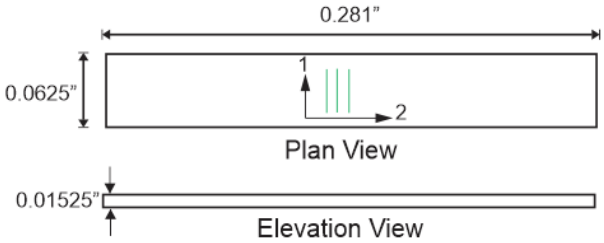


Figure 5.11: 2-direction Tension Virtual Test Specimen Layout

*Boundary Condition and Model Details*

The black colored nodes in Figure 5.12 are restrained in the X, Y and Z directions. The red colored nodes are restrained in the Y direction. The blue colored nodes have displacements applied in the positive Y direction.

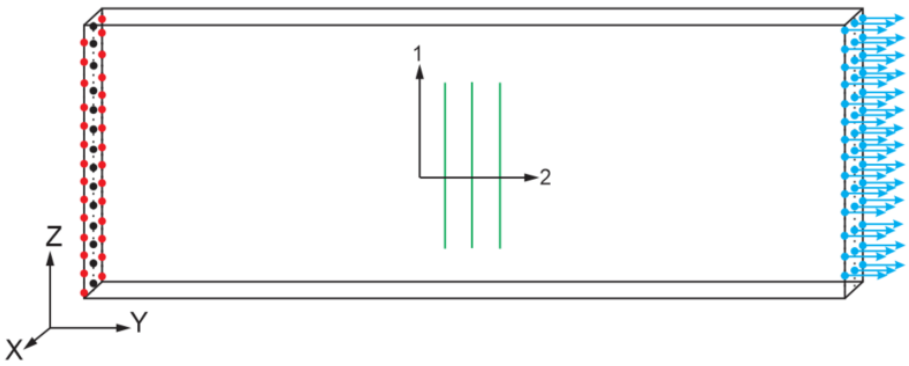


Figure 5.12: Boundary Conditions for 2-direction Tension

The VTSS geometric parameter details for different meshes are provided in Table 5.4. The total number of nodes, elements, maximum and minimum aspect ratio are provided in Table 5.5. Figure 5.13 shows the top view and isometric view of the virtual test specimen.

Table 5.4: VTSS Geometric Parameter Details for 2-direction Tension Test Models

| **Model** | $a$ **(in)** | $r$ **(in)** | $\alpha$ | $dxy$ **(in)** | $dz$ **(in)** | $L$ **(in)** | **# Rows** | **# Columns** |
|---|---|---|---|---|---|---|---|---|
| CM | 0.0076 | 0.0033 | 22.5 | 0.00166 | 0.0024 | 0.0625 | 37 | 2 |
| MM | 0.0076 | 0.0033 | 22.5 | 0.00166 | 0.0018 | 0.0625 | 37 | 2 |
| FM | 0.0076 | 0.0033 | 22.5 | 0.00166 | 0.0012 | 0.0625 | 37 | 2 |

Table 5.5: Model Details for 2-direction Tension Test Models

| **Model** | **# Elements** | **# Nodes** | **Max. AR** | **Min. AR** |
|---|---|---|---|---|
| CM | 95904 | 87276 | 4.823 | 2.914 |
| MM | 124320 | 112212 | 3.72 | 2.745 |
| FM | 188256 | 168318 | 3.29 | 2.56 |

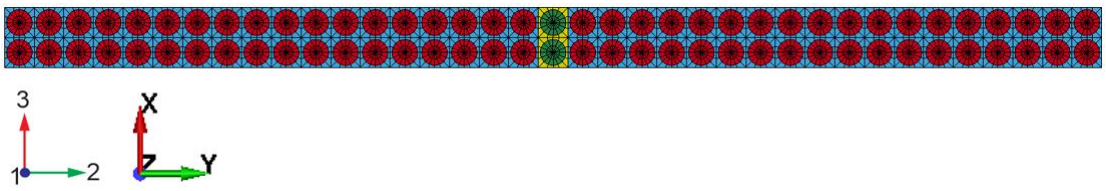


(a)

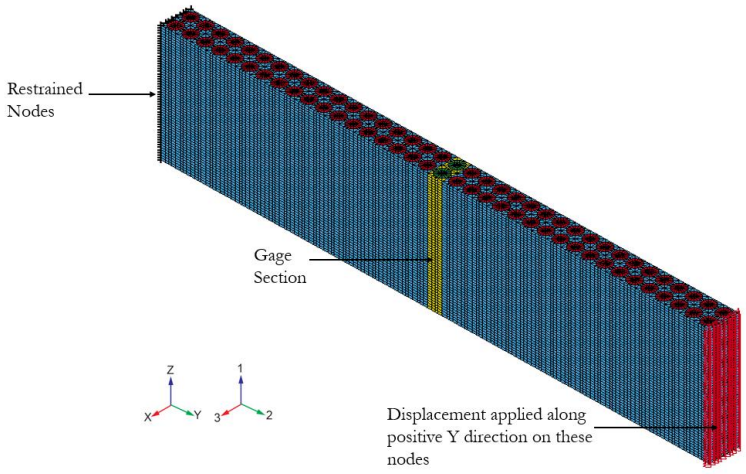


(b)

Figure 5.13: 2-direction Tension Fine Model (a) Top View (b) Isometric View

*Deformation only 2-direction Tension Results*

The 2-direction tension test results for all the three virtual test models (CM, MM and FM) are shown in Figure 5.14. The deformation only response from all the three specimens is same. The LS-DYNA plot of the kinetic energy, internal energy and total energy for the FM is shown in Figure 5.15. The response of the virtual test specimens is slightly stiffer compared to the *Model Curve*.

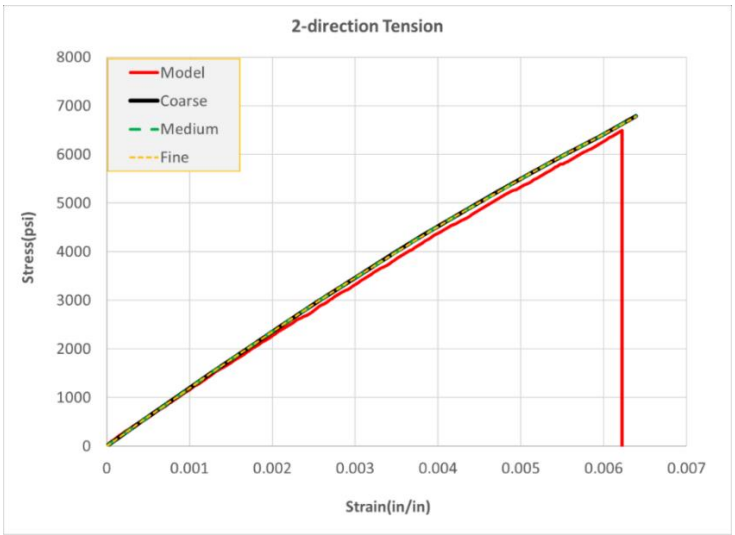


Figure 5.14: Deformation only 2-direction Tension Response

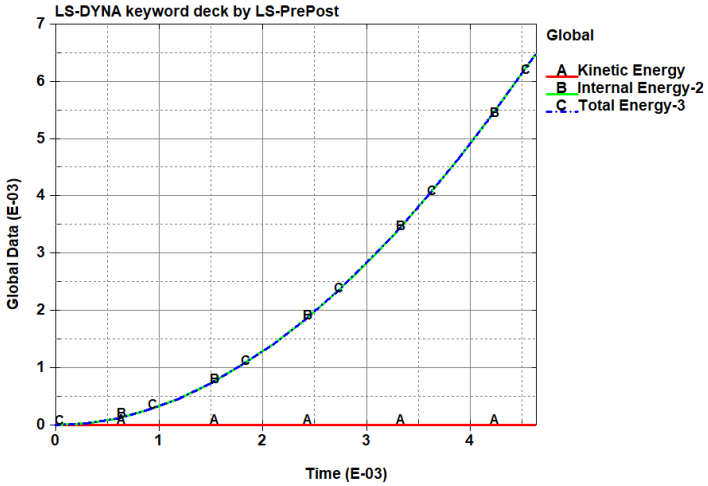

Figure 5.15: LS-DYNA Energy Plots for 2-direction Tension

The contour plot of Y stresses, where Y direction is the loading direction, in the fiber and the matrix elements of the FM corresponding to homogenized composite Y stress of 6390 psi in Figure 5.14 is shown in Figure 5.16a. The Y stresses in the matrix elements in and in the fiber elements are maximum along the loading direction. In the matrix elements, along the direction perpendicular to the loading, they are $1/10^{th}$ of the maximum Y stresses. In Figure 5.16b, the Y strains in the fiber are approximately $1/10^{th}$ of the Y strains in the matrix elements. At the same time step, the contour plot of the Y stresses in the fiber and the matrix elements in the gage section is shown in Figure 5.17. The Y stresses in the matrix elements near the top and the bottom edge and near the left and the right edge are low compared to the stresses in the matrix elements away from the edges.

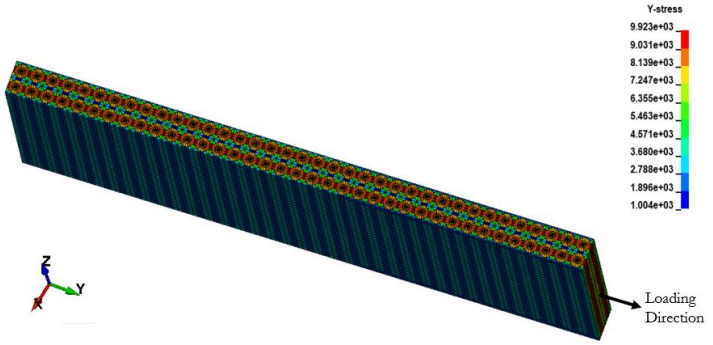


(a)

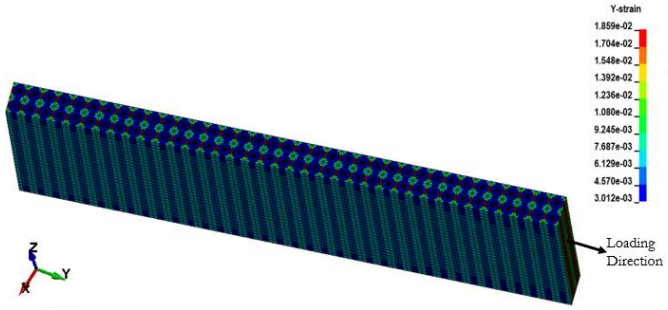


(b)

Figure 5.16: LS-DYNA Y Stress Contour Plots for 2-direction Tension (a) Stress(psi) (b) Strain (in/in)

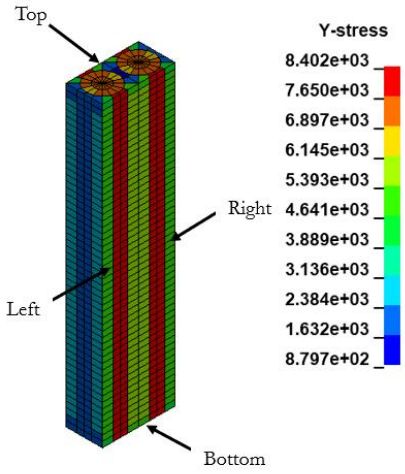


Figure 5.17: LS-DYNA Y-Stress Contour Plots of the Gage Section for 2-direction Tension

*Deformation and Failure 2-direction Tension Test Results*

The 2-direction tension test results for all the three virtual test models are shown in Figure 5.18. The failure stress, failure strain and failure mode from all the three models were nearly same.

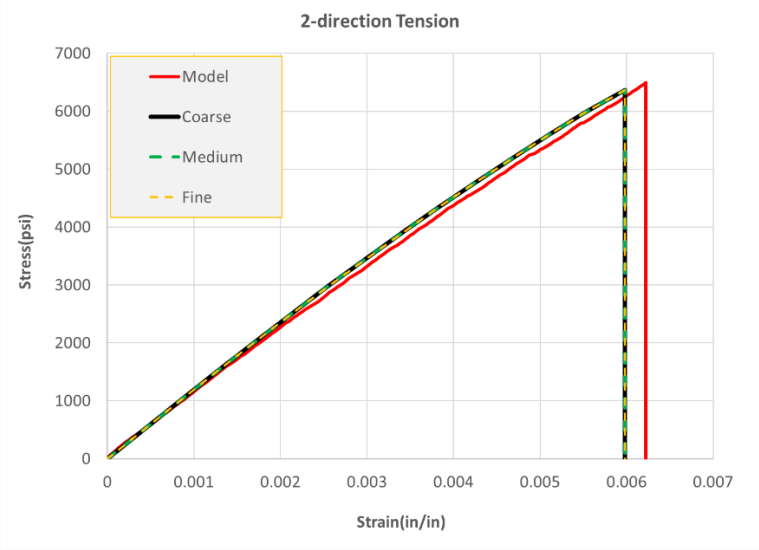


Figure 5.18: Deformation and Failure for 2-direction Tension

The 2-direction tension FM before failure is shown in Figure 5.19a and after failure is shown in Figure 5.19b and 5.19c. The failure initiates in the matrix elements near the loading edge (Figure 5.19b). Two failure zones are highlighted in Figure 5.19c with red box. The second failure zone is due to the snapping back of the specimen.

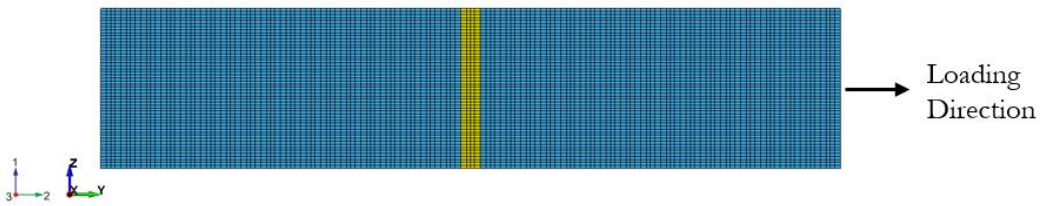


(a)

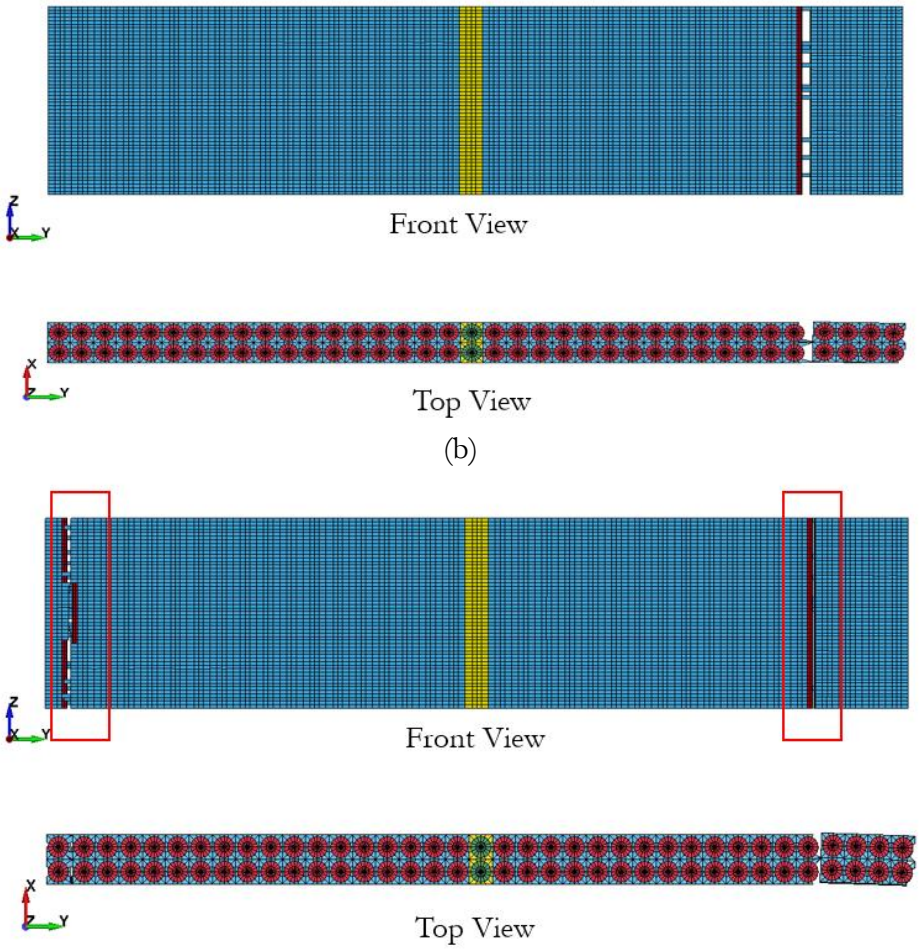


Figure 5.19: 2-direction Tension Fine Specimen (a) Specimen without Failure (b) Failure Initiation in Specimen (c) Failed Specimen

## 5.3 1-direction Compression

*Virtual Test Specimen Geometry*

The experimental specimen layout is shown in Figure 5.20, where the shaded region represents the area where fiber glass tabs were used. The experimental specimen is a flat specimen with through thickness of 0.122" such that $\left(1:\frac{L}{t}:\frac{w}{t}=1:6.14:6.14\right)$. Figure 5.21 shows the virtual test specimen with the equivalent dimensions. The through thickness of

the virtual test specimen is 0.01525" such that $\left(1:\frac{L}{t}:\frac{w}{t}=1:6.1:6.1\right)$. In virtual test specimen, the tab sections are not modeled.

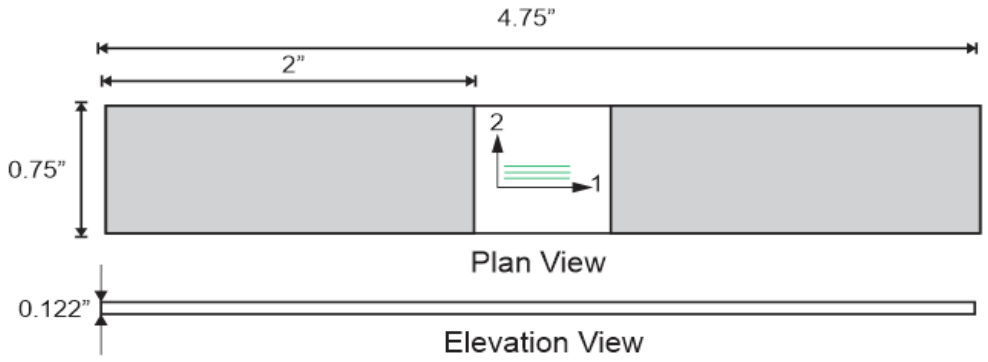


Figure 5.20: 1-direction Compression Experimental Specimen Layout

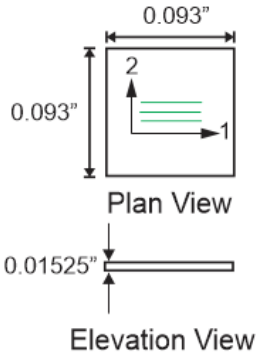


Figure 5.21: 1-direction Compression Virtual Test Specimen Layout

*Boundary Conditions and Model Details*

The black colored nodes in Figure 5.22 are restrained in the X, Y and Z directions. The red colored nodes are restrained in the Z direction. The blue colored nodes have displacements applied along the negative Z direction.

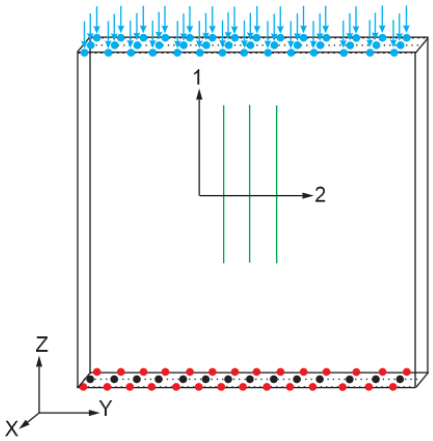


Figure 5.22: Boundary Conditions for 1-direction Compression

The VTSS geometric parameter details for different meshes are provided in Table 5.6. The total number of nodes, elements, maximum and minimum aspect ratio are provided in Table 5.7. Figure 5.23 shows the top view and the isometric view of the virtual test specimen.

Table 5.6: VTSS Geometric Parameter Details for 1-direction Compression Test Models

| **Model** | $a$ **(in)** | $r$ **(in)** | $\alpha$ | $dxy$ **(in)** | $dz$ **(in)** | $L$ **(in)** | **# Rows** | **# Columns** |
|---|---|---|---|---|---|---|---|---|
| CM | 0.0076 | 0.00333 | 22.5 | 0.00166 | 0.0024 | 0.0939 | 2 | 13 |
| MM | 0.0076 | 0.00333 | 22.5 | 0.00166 | 0.0018 | 0.0939 | 2 | 13 |
| FM | 0.0076 | 0.00333 | 22.5 | 0.00166 | 0.0012 | 0.0939 | 2 | 13 |

Table 5.7: Model Details for 1-direction Compression Test Models

| **Model** | **# Elements** | **# Nodes** | **Max. AR** | **Min AR** |
|---|---|---|---|---|
| CM | 49920 | 45141 | 4.894 | 2.958 |
| MM | 66144 | 59454 | 3.69 | 2.728 |
| FM | 98592 | 88080 | 3.29 | 2.56 |

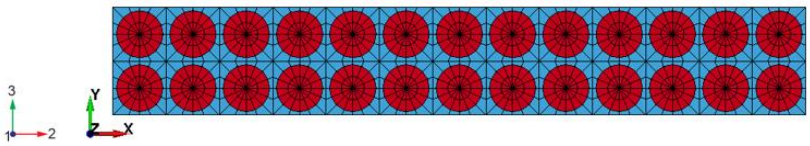


(a)

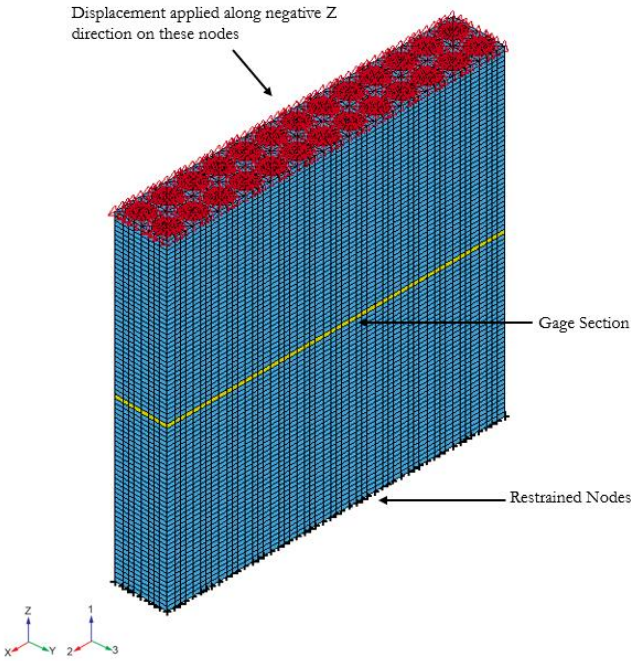


(b)

Figure 5.23: 1-direction Compression Fine Model (a) Top View (b) Isometric View

*Deformation Only 1-direction Compression Results*

The direction of the loading is along negative Z direction. The contour plot of Z stresses in the fiber and the matrix of the gage section for the FM corresponding to the homogenized composite Z stress of 100000 psi is shown in Figure5.24, is shown in Figure 5.26a. The Z stresses in the fiber and the matrix elements are uniform throughout the width of the gage section. The Z stresses in the fiber elements are higher by two orders of magnitude compared to the Z stresses in the matrix elements. The contribution of the matrix elements in resisting loads in 1-direction compression is negligible compared to the

fiber elements. The contour plot of Z strains in the gage section is shown in Figure 5.26b. The Z strains in the fiber and the matrix elements are same and uniform throughout the width of the gage section.

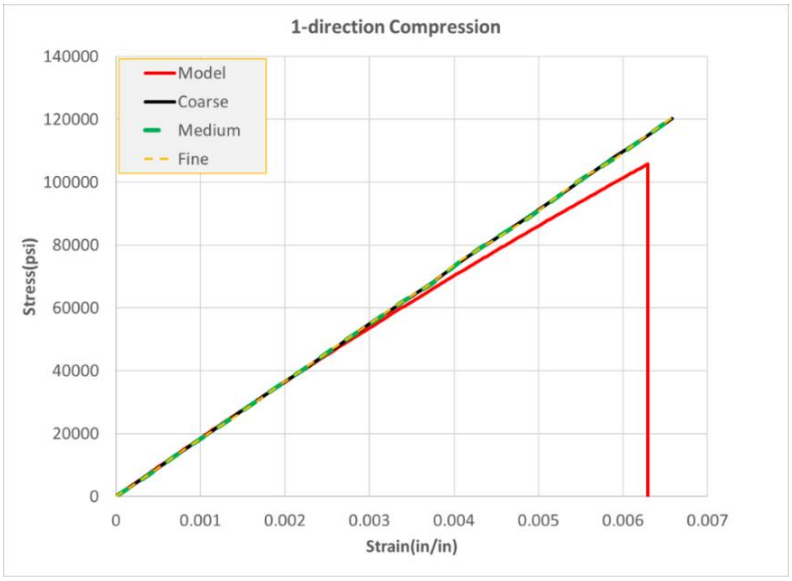


Figure 5.24: Deformation Only 1-direction Compression Response

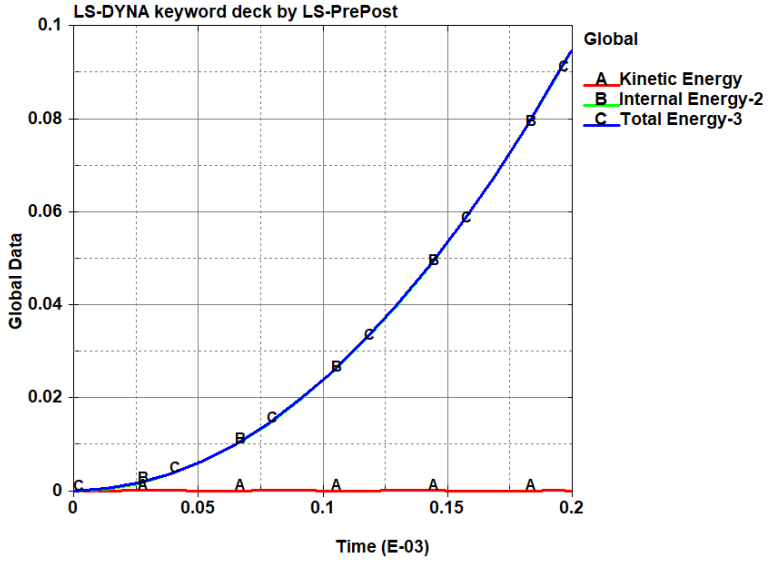


Figure 5.25: LS-DYNA Energy Plots for 1-direction Compression

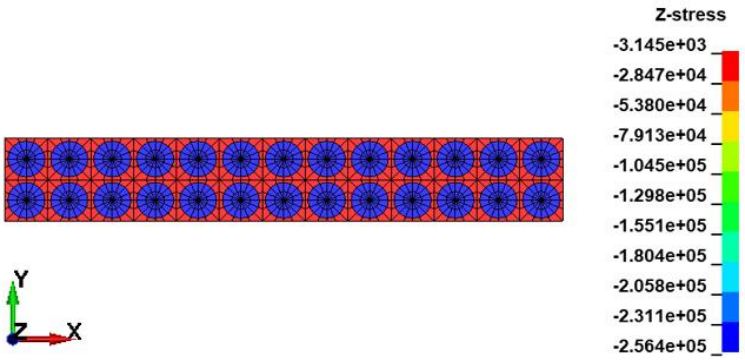


(a)

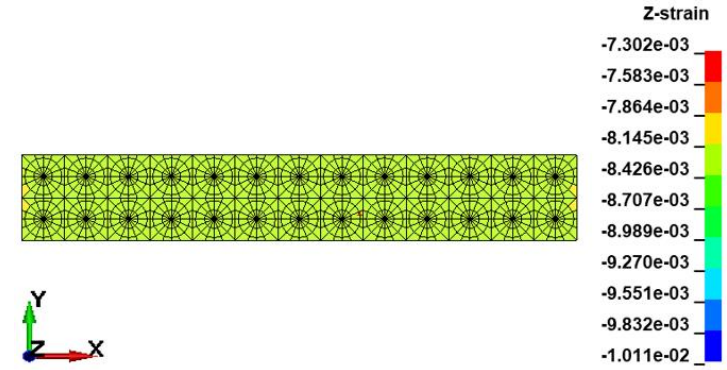


(b)

Figure 5.26: LS-DYNA Contour Plots for 1-direction Compression (a) Z Stress(psi) (b)Z Strain (in/in)

*Deformation and Failure 1-direction Compression Results*

The 1-direction compression test results for all the three virtual test models (CM, MM and FM) are shown in Figure 5.27. The failure stress and failure strain for the FM is higher compared to CM and MM. The failure pattern in CM and MM are the same, however the failure pattern in FM is different. The failure pattern in 1-direction compression MM is shown in Figure 5.28b. Figure 5.28a is MM before failure. The failure pattern in the fiber elements is shown in Figure 5.28c and in the matrix elements in Figure 5.28d. In Figure 5.28b, four failure zones are highlighted with different colored box. The failure initiates in the fiber elements on the loading edge highlighted by red box and as the loading progresses,

the fibers around the central region highlighted by black box fail as shown in Figure 5. 28c along with the failure of the matrix elements. The matrix elements fail along the direction of the fiber highlighted by green box.

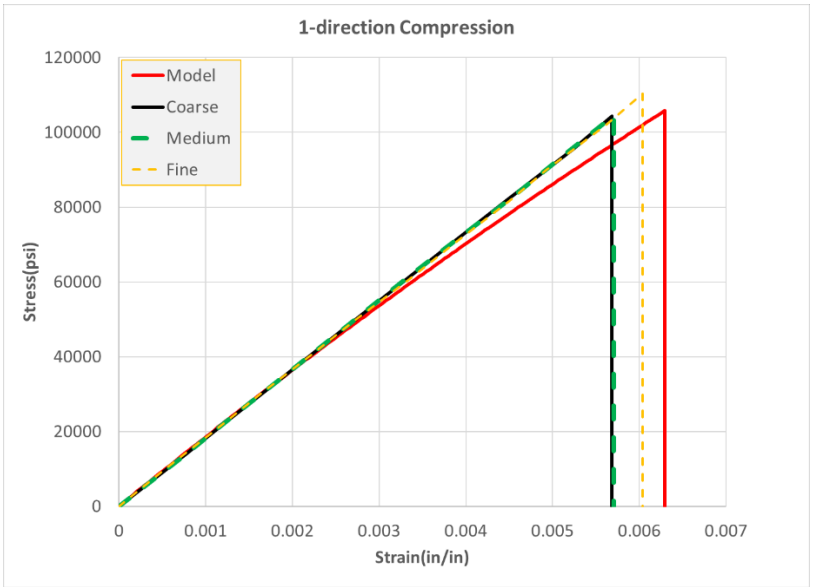


Figure 5.27: Deformation and Failure for 1-direction Compression

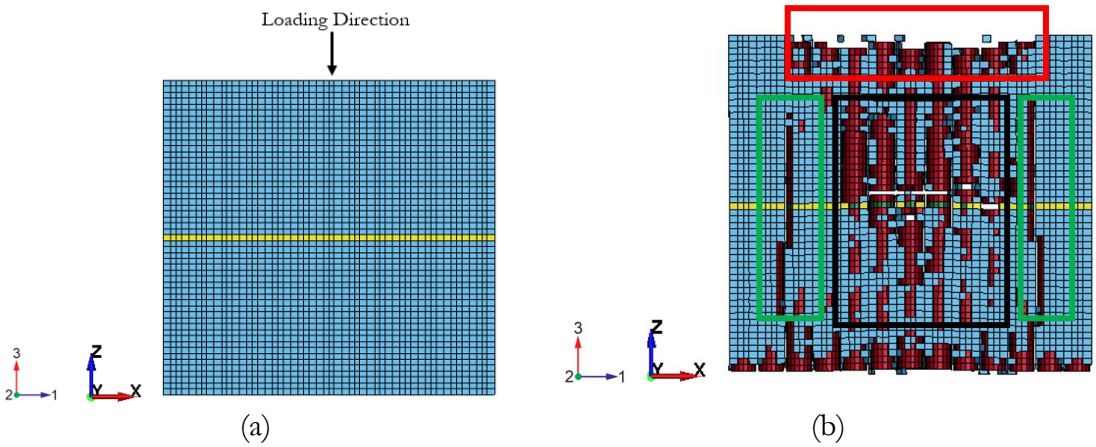

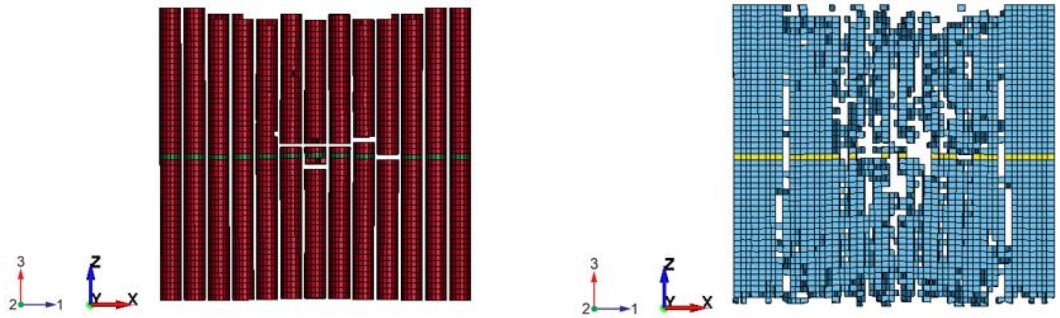


(c) (d)

Figure 5.28: 1-direction Compression Medium Specimen (a) Specimen without Failure (b) Failed Specimen(c) Failure in Fiber Elements (d) Failure in Matrix Elements

The failure pattern in 1-direction compression FM is shown in Figure 5.29a. The failure pattern in the fiber elements is shown in Figure 5.29b and in the matrix elements in Figure 5.29c. The failure initiated in the fiber elements on the loading edge as highlighted with red box in Figure 5.29b. After all the fiber elements near the loading edge fail, the load is transferred to the specimen through excessive crushing of the matrix elements near the loading edge as highlighted by red box in Figure 5.29c. This is followed by failure of the fiber elements near the fixed edge as highlighted with the blue box in Figure 5.29b. The delayed failure in FM is due to the load transfer through the matrix elements near the loading edge.

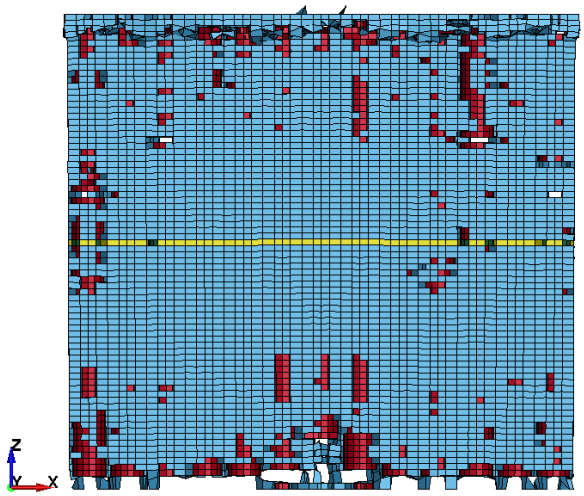

(a)

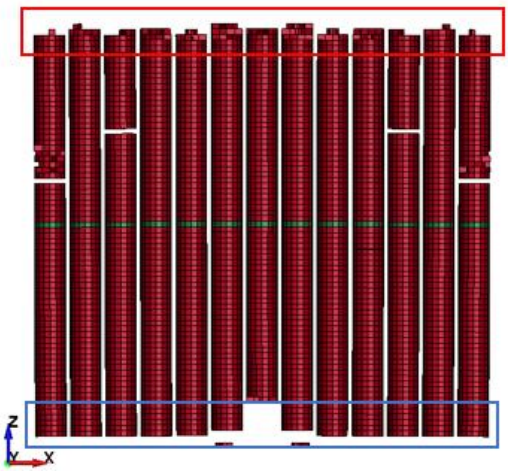

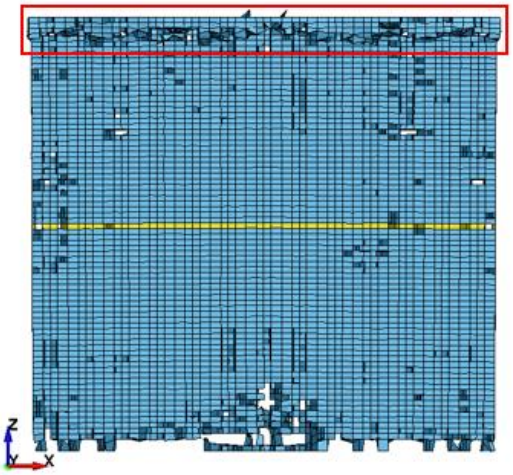

(b) (c)

Figure 5.29: 1-direction Compression Fine Specimen (a) Failed Specimen (b) Failure in Fiber Elements (c) Failure in Matrix Elements

## 5.4 2-direction Compression

*Virtual Test Specimen Geometry*

The experimental specimen layout is shown in Figure 5.30, where the shaded region represents the area where fiber glass tabs were used. The experimental specimen is a flat specimen with through thickness of 0.122" such that $\left(1:\frac{L}{t}:\frac{w}{t}=1:6.14:8.2\right)$. Figure 5.31

shows the virtual test specimen with the equivalent dimensions. The through thickness of the virtual test specimen is 0.01525" such that $\left(1:\frac{L}{t}:\frac{w}{t}=1:6.4:8.2\right)$. In virtual test specimen, the tab sections are not modeled.

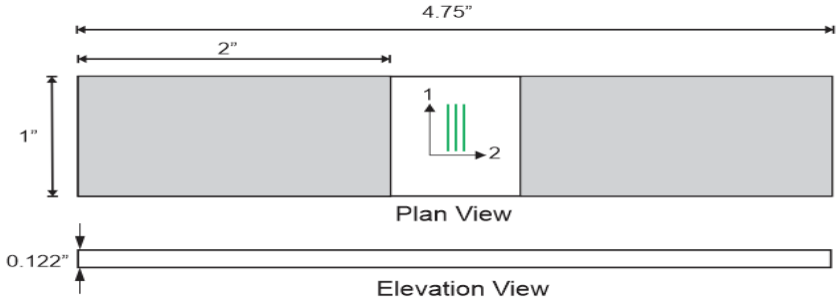


Figure 5.30: 2-direction Compression Experimental Specimen Layout

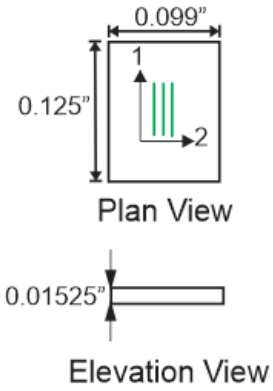


Figure 5.31: 2-direction Compression Virtual Test Specimen Layout

*Boundary Conditions and Model Details*

The black colored nodes in Figure 5.32 are restrained in the X direction. The red colored nodes are restrained in the Z direction. The green colored nodes are restrained in the Y direction. The blue colored nodes have displacements applied along the negative Y direction. These boundary conditions were used to prevent the out-of-plane buckling of the specimen.

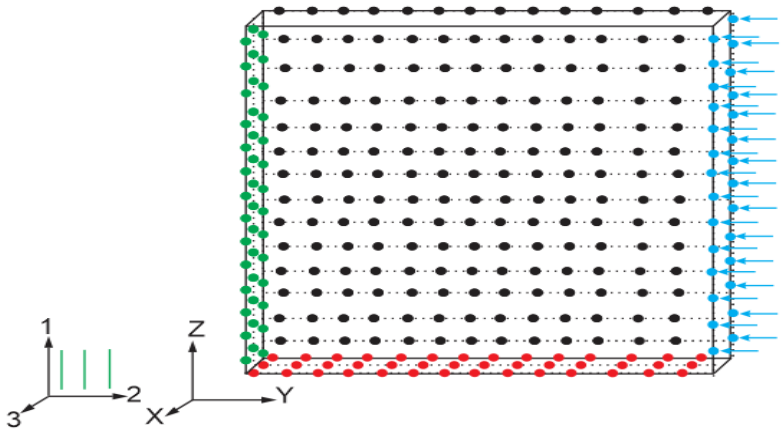


Figure 5.32: Boundary Conditions for 2-direction Compression

The VTSS geometric parameter details for different meshes are provided in Table 5.8. The total number of nodes, elements, maximum and minimum aspect ratio are provided in Table 5.9. Figure 5.33 shows the top view and the isometric view of the virtual test specimen.

Table 5.8: VTSS Geometric Parameter Details for 2-direction Compression Test Models

| **Model** | *a* **(in)** | *r* **(in)** | *α* | *dxy* **(in)** | *dz* **(in)** | *L* **(in)** | **# Rows** | **# Columns** |
|---|---|---|---|---|---|---|---|---|
| CM | 0.0076 | 0.00333 | 22.5 | 0.001666 | 0.0024 | 0.125 | 13 | 2 |
| MM | 0.0076 | 0.00333 | 22.5 | 0.001666 | 0.0018 | 0.125 | 13 | 2 |
| FM | 0.0076 | 0.00333 | 22.5 | 0.001666 | 0.0012 | 0.125 | 13 | 2 |

Table 5.9: Model Details for 2-direction Compression Test Models

| **Model** | **# Elements** | **# Nodes** | **Max. AR** | **Min. AR** |
|---|---|---|---|---|
| CM | 66144 | 59454 | 4.91 | 2.968 |
| MM | 87360 | 78171 | 3.71 | 2.74 |
| FM | 131040 | 116706 | 3.29 | 2.56 |

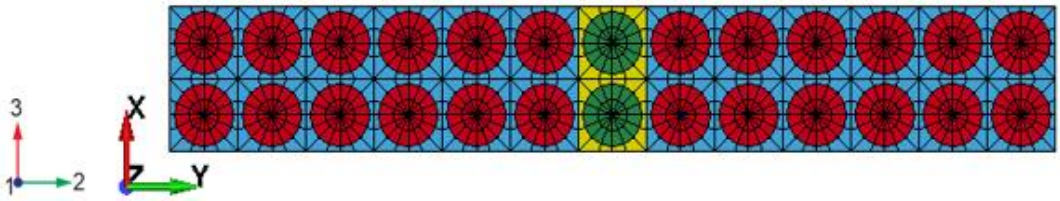


(a)

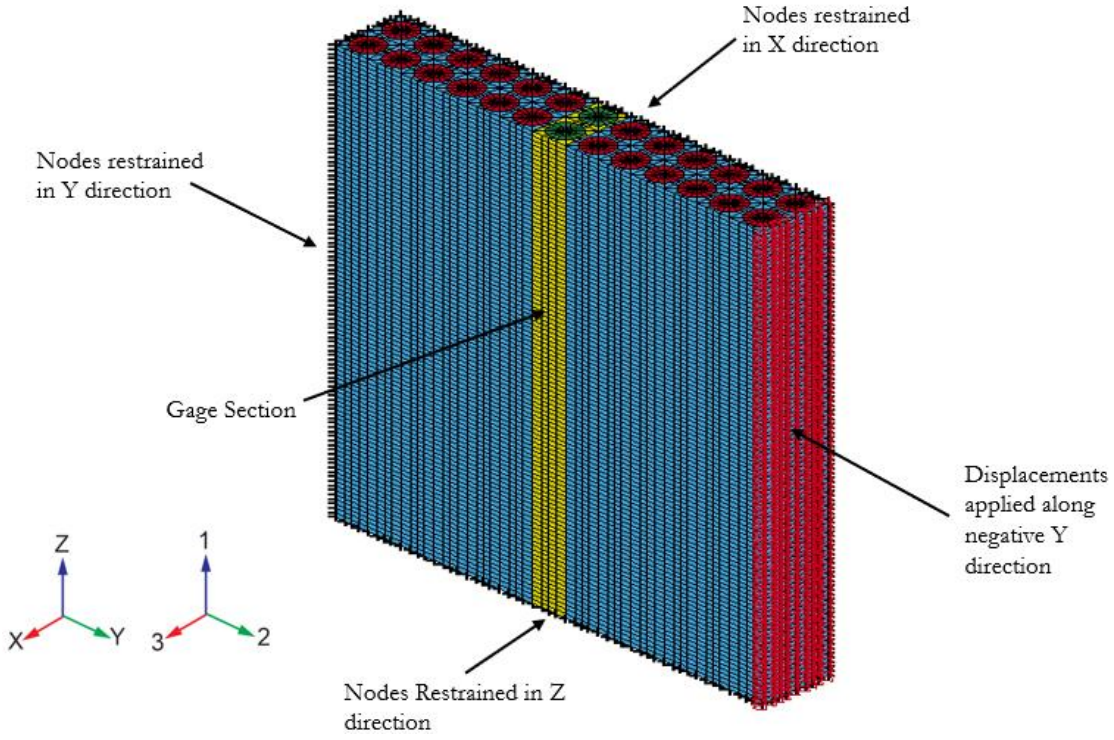


(b)

Figure 5.33: 2-direction Compression Fine Model (a) Top View (b) Isometric View

*Deformation Only 2-direction Compression Results*

The 2-direction compression test results for all the three virtual test models (CM, MM and FM) are shown in Figure 5.34. The deformation only response from all the three models are same until the strain of 0.0198. The matrix elements in the CM and the MM specimen start distorting excessively thereby leading to significant decrease in the time step in the analysis. The problem of the excessive deformation of the matrix elements is similar to

the soft material between two rigid materials under compression. One of the solutions to prevent this is by improving the mesh density and the aspect ratio. The FM specimen has better aspect ratio compared to the CM and MM specimen and hence the excessive deformation in the matrix elements were not observed until the strain of 0.048. The LS-DYNA plot of the kinetic energy, internal energy and total energy for FM is shown in Figure 5.35.

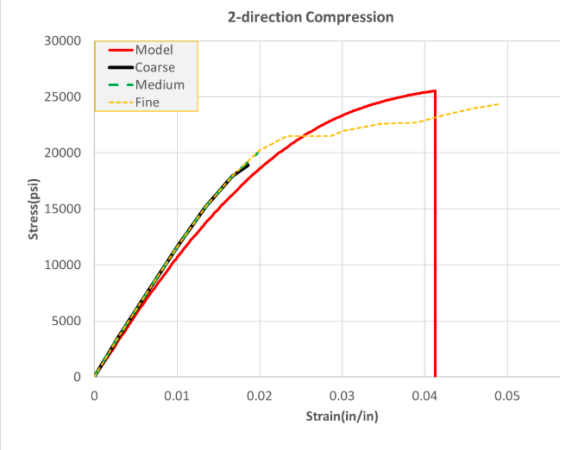


Figure 5.34: Deformation Only 2-direction Compression Response

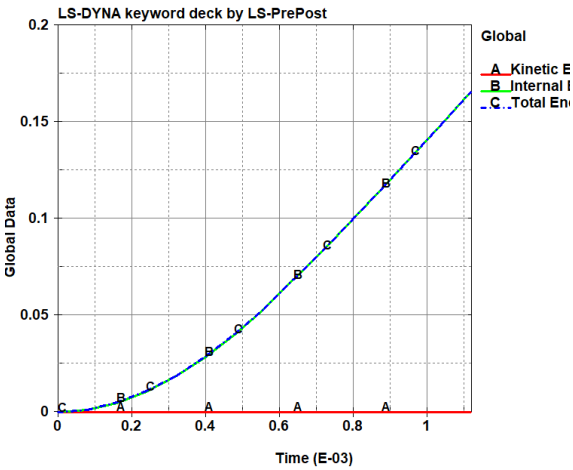


Figure 5.35: LS-DYNA Energy Plots for 2-direction Compression

The stress and strain distribution in the matrix elements and the fiber elements is very similar to the 2-direction tension, where the Y stresses in the matrix elements and the fiber elements are maximum along the loading direction and decrease in the elements perpendicular to the loading direction as shown in Figure 5.36a. The stress and strain contours in Figure 5.36 are for the time step corresponding to the stress of 17000 psi in Figure 5.34 for the FM. The Y strain in the matrix elements are maximum along the loading direction and an order of magnitude lower along the direction perpendicular to the loading

direction. The Y strains in the fiber elements are uniform and approximately lower by an order of magnitude compared to the maximum Y strains in the matrix elements as shown in Figure 5.35b.

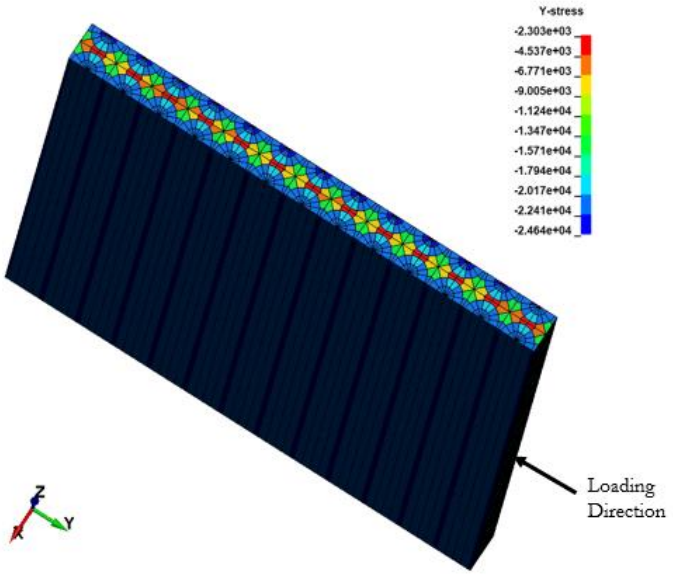


(a)

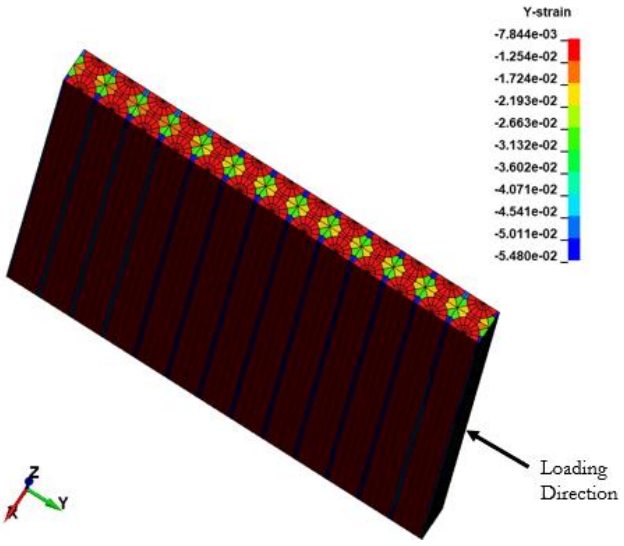


(b)

Figure 5.36: LS-DYNA Contour Plot in 2-direction Compression (a) Y Stress (psi) (b) Y Strain (in/in)

*Deformation and Failure 2-direction Compression Results*

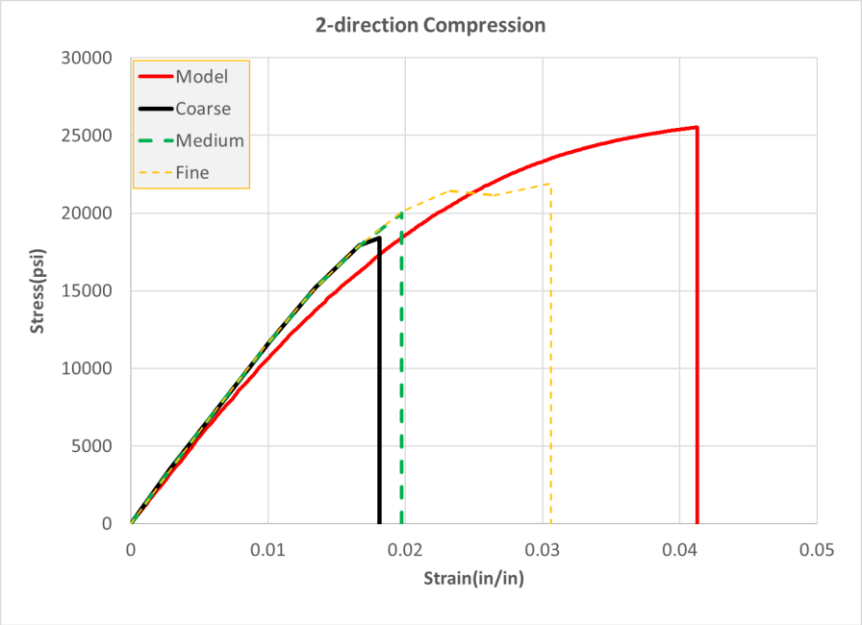


Figure 5.37: Deformation and Failure for 2-direction Compression

The 2-direction compression test results for all the three virtual test models: CM, MM and FM are shown in Figure 5.37. The failure stress and failure strain for the fine model is higher compared to the failure strain of the CM and MM. The failure strain in CM and MM corresponds to the stresses at which the matrix elements start deforming excessively.

The specimen before failure is shown in Figure 5.38a. The front view of the specimen at the failure initiation is shown in Figure 5.38b and the back view is shown in Figure 5.38c. The failure initiates in the matrix elements as shown in the isometric view of Figure 5.38d and highlighted with black circles in the top view.

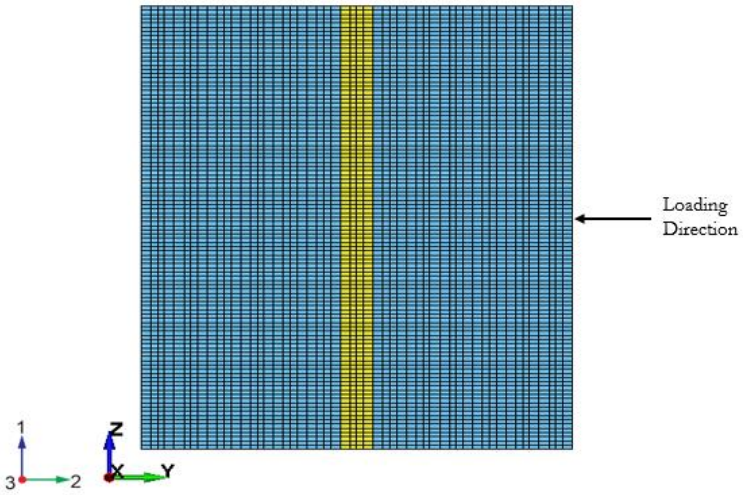


(a)

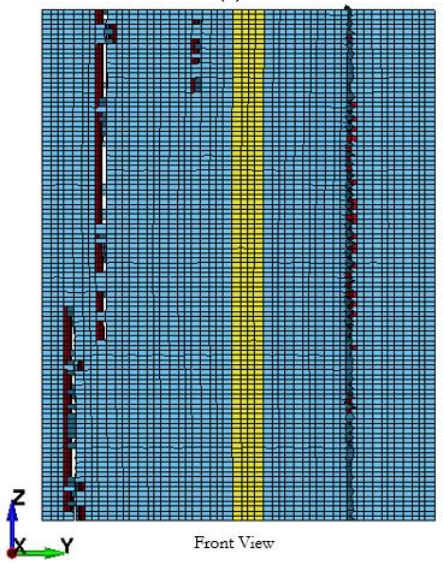


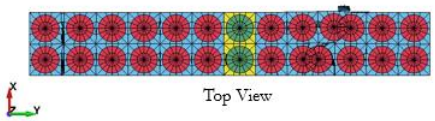


(b)

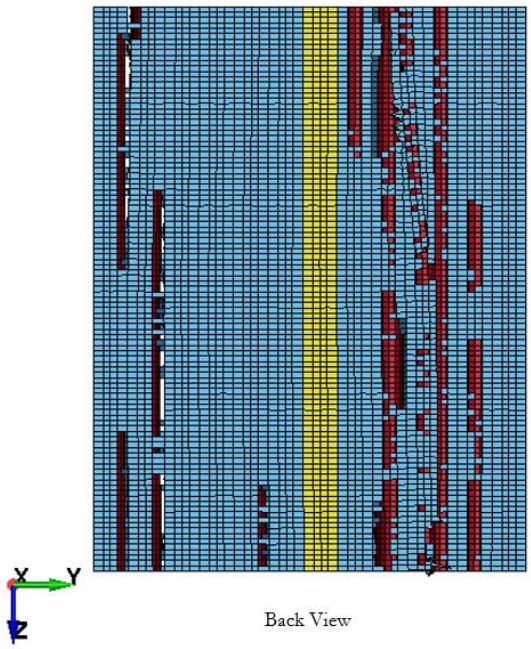


(c)

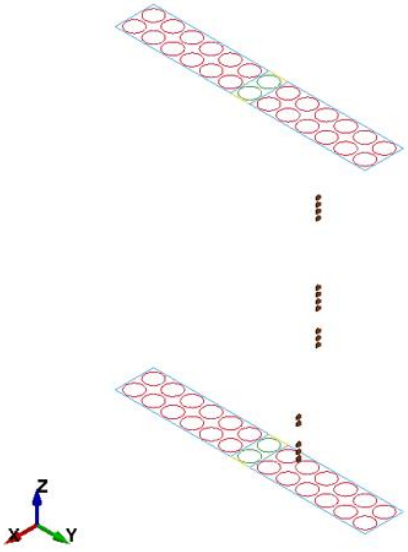


(d)

Figure 5.38: 2-direction Compression Fine Specimen (a) Specimen Before Failure (b) Front View, Bottom View and Top View of the Specimen (c) Back View of the Specimen (d) Failure Initiation in the Matrix Elements

5.5 2-1 Plane Shear

*Virtual Test Specimen Geometry*

The experimental specimen layout is shown in Figure 5.39 where the shaded region represents the area where fiber glass tabs were used. The experimental specimen is a flat specimen with through thickness of 0.185" such that $\left(1:\frac{L}{t}:\frac{w}{t}=1:2.7:4\right)$. Figure 5.40 shows the virtual test specimen with the equivalent dimensions. The through thickness of the virtual test specimen is 0.015416" such that $\left(1:\frac{L}{t}:\frac{w}{t}=1:2.5:4\right)$. In virtual test specimen, the tab sections are not modeled.

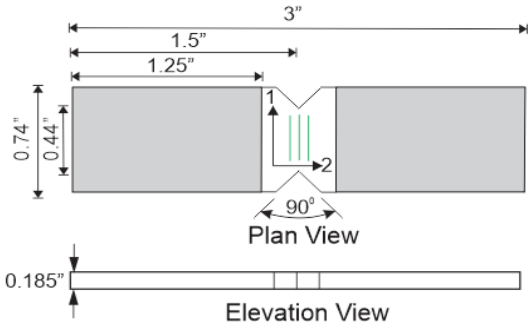


Figure 5.39: 2-1 plane Shear Experimental Specimen Layout

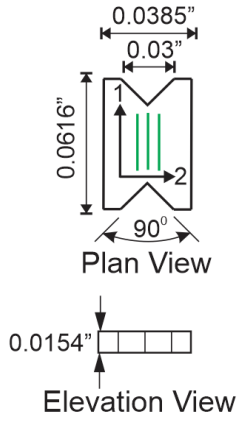


Figure 5.40: 2-1 plane Shear Virtual Test Specimen Layout

*Boundary Conditions and Model Details*

The black colored nodes in Figure 5.41 are restrained in the X, Y and Z directions. The blue colored nodes have displacements applied along the positive Z direction. The blue colored nodes are also restrained in the Y direction.

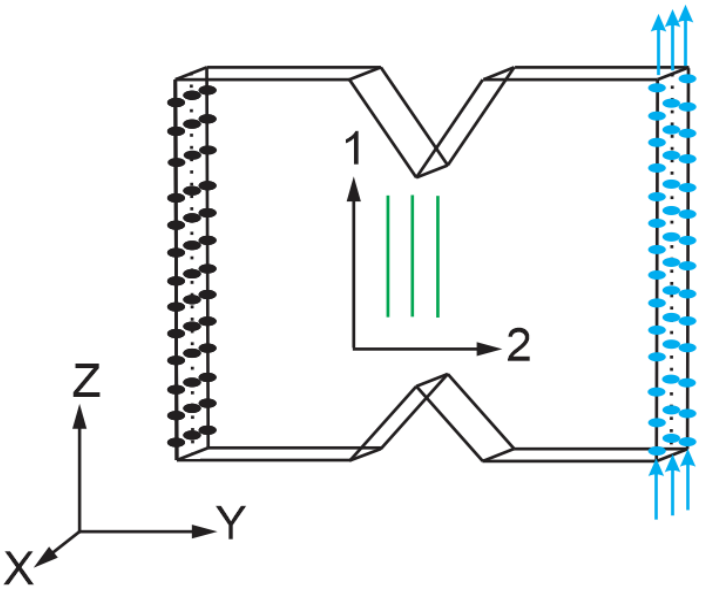


Figure 5.41: Boundary Conditions for 2-1 plane Shear

The VTSS geometric parameter details for different meshes are provided in Table 5.10. The total number of nodes, elements, maximum and minimum aspect ratio are provided in Table 5.11. Figure 5.42 shows the top view and the isometric view of the virtual test specimen.

Table 5.10: VTSS Geometric Parameter Details for 2-1 plane Shear Test Models

| **Model** | *a* **(in)** | *r* **(in)** | *α* | *dxy* **(in)** | *dz* **(in)** | *L* **(in)** | **# Rows** | **# Columns** |
|---|---|---|---|---|---|---|---|---|
| CM | 0.0077 | 0.00336 | 22.5 | 0.00168 | 0.0024 | 0.06167 | 5 | 2 |
| MM | 0.0077 | 0.0033 | 22.5 | 0.00168 | 0.0018 | 0.06167 | 5 | 2 |
| FM | 0.0077 | 0.0033 | 22.5 | 0.00168 | 0.0012 | 0.06167 | 5 | 2 |

Table 5.11: Model Details for 2-1 plane Shear Test Models

| Model | # Elements | # Nodes | Max. AR | Min AR |
|---|---|---|---|---|
| CM | 10014 | 9631 | 4.88 | 2.95 |
| MM | 13904 | 13103 | 3.73 | 2.76 |
| FM | 19824 | 18604 | 3.284 | 2.56 |

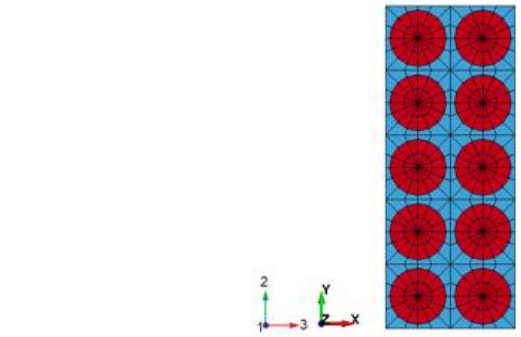


(a)

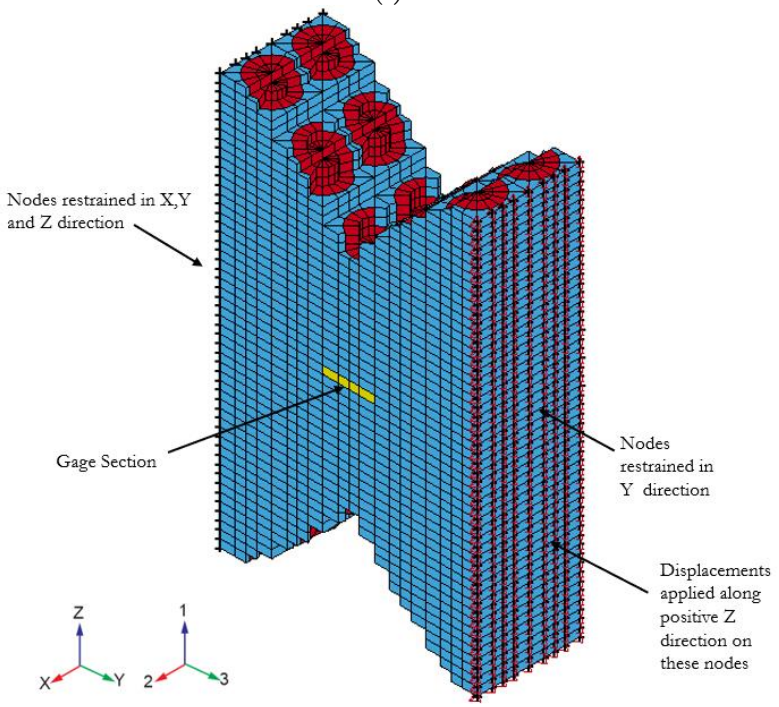


(b)

Figure 5.42: 2-1 plane Shear Fine Model (a) Top View (b) Isometric View

*Deformation Only 2-1 plane Shear Results*

The 2-1 plane shear test results for all the three virtual test models: CM, MM and FM are shown in Figure 5.43. The deformation only response of the CM and FM is same. The response of the MM is slightly softer in the non-linear region compared to the CM and the FM response. The LS-DYNA plot of the kinetic energy, internal energy and the total energy for the FM is shown in Figure 5.44.

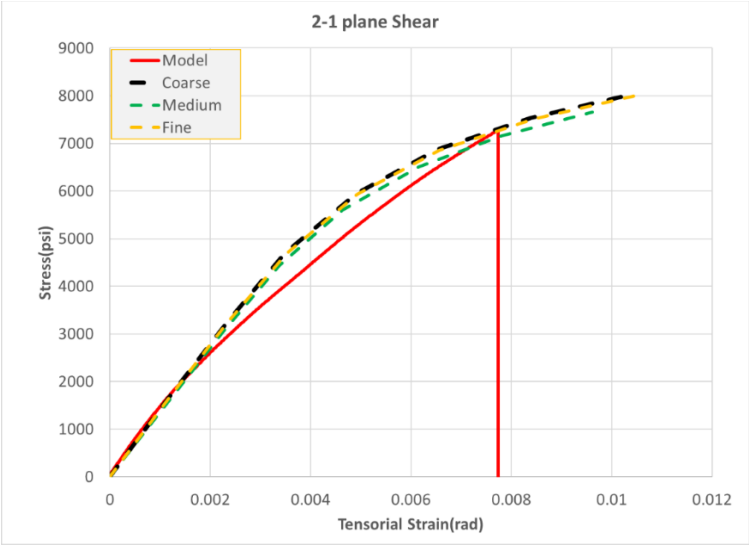


Figure 5.43: Deformation Only 2-1 plane Shear Response

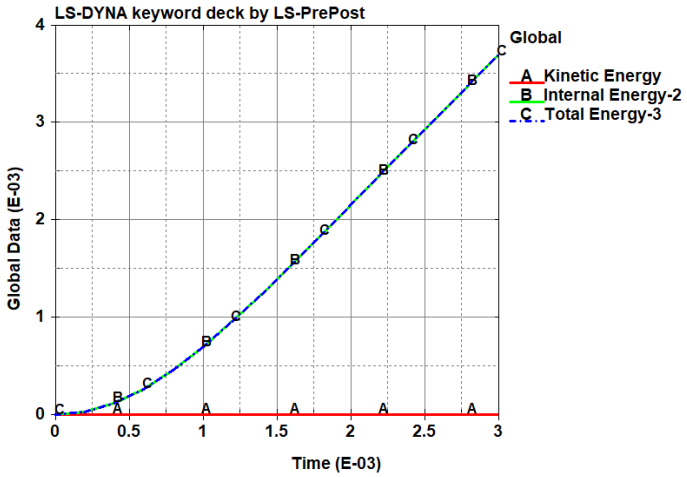


Figure 5.44: LS-DYNA Energy Plots for 2-1 plane Shear

The contour plot of YZ stresses in the fiber and the matrix of the gage section for the FM for the time step corresponding to the homogenized composite YZ stress of 7000 psi (Figure 5.43) is shown in Figure 5.45a and 5.45b respectively. The YZ max. stresses in fiber are near the central region below the notch. The YZ max. stresses in the matrix are around the central region but the YZ stresses in the matrix elements in the center and below the notches are comparatively lower. The YZ stress distribution in the gage section is shown in Figure 5.45c. The YZ stresses in the matrix elements along X direction are the least and increase in the matrix along Y direction. The reverse trend in observed in the fiber elements. The YZ stresses in the fiber elements are an order of magnitude higher compared to the YZ stresses in the matrix elements.

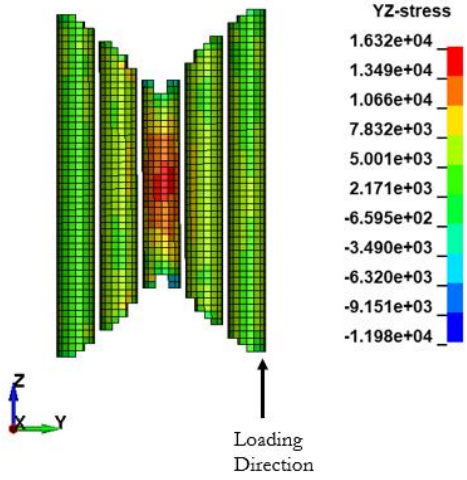


(a)

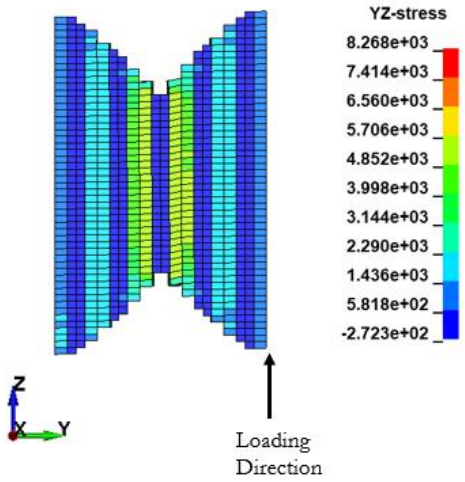


(b)

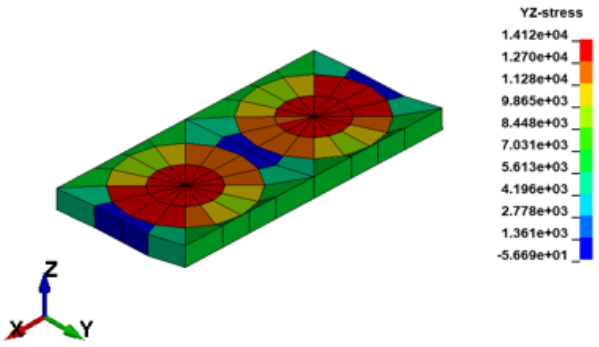


(c)

Figure 5.45: LS-DYNA YZ Stress Contour Plots for 2-1 plane Shear (a) Fiber (b) Matrix (c) Gage Section

The YZ strain contour plots of the fiber and the matrix elements at the same time step are shown in Figure 5.46a and Figure 5.46b respectively. The YZ strain in the fiber elements are maximum near the central region below the notches. In case of the matrix elements, the YZ strains are maximum in the matrix elements just to the right of the notch center. This is because of the fibers being present just below the notch. The YZ strains in the fiber elements are lower by order of magnitude 2 compared to the maximum strain in the matrix elements. In Figure 5.46c, the YZ strains in the fiber elements are uniform. The YZ strain in the matrix elements near the loading edge are maximum and low in the matrix elements along X direction.

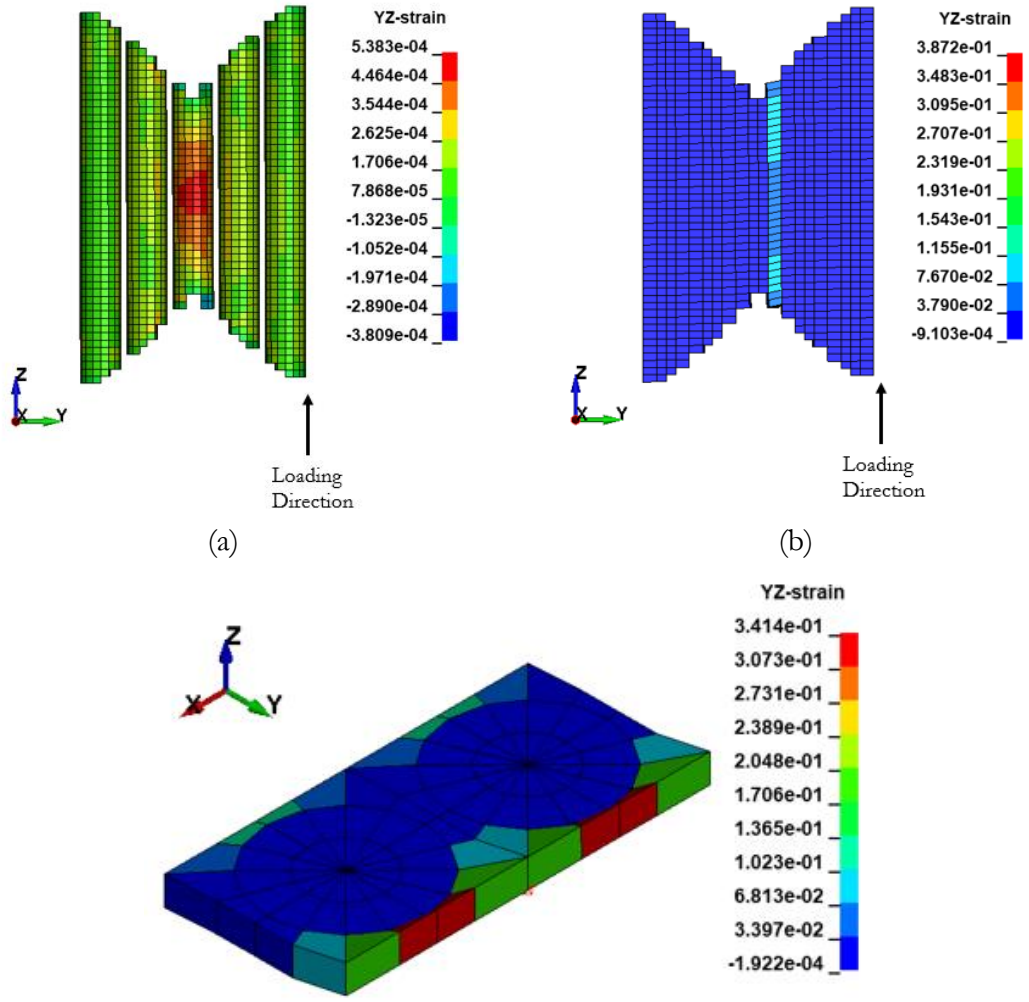


Figure 5.46: LS-DYNA YZ Strain Contour Plots for 2-1 plane Shear (a) Fiber (b) Matrix (c) Gage Section

*Deformation and Failure 2-1 plane Shear Results*

The 2-1 plane shear test results for all the three virtual test models: CM, MM and FM are shown in Figure 5.47. The failure stress and failure strain for the FM and the CM is higher compared to the failure stress and strain of the MM. The failure pattern for CM, MM and FM are different. The failure pattern for CM, MM and FM are shown in Figure 5.48a,

5.48b and 5.48c respectively. The failures of the CM and MM are near the boundary and away from the notches. However, the failure of the FM is at the notch edge.

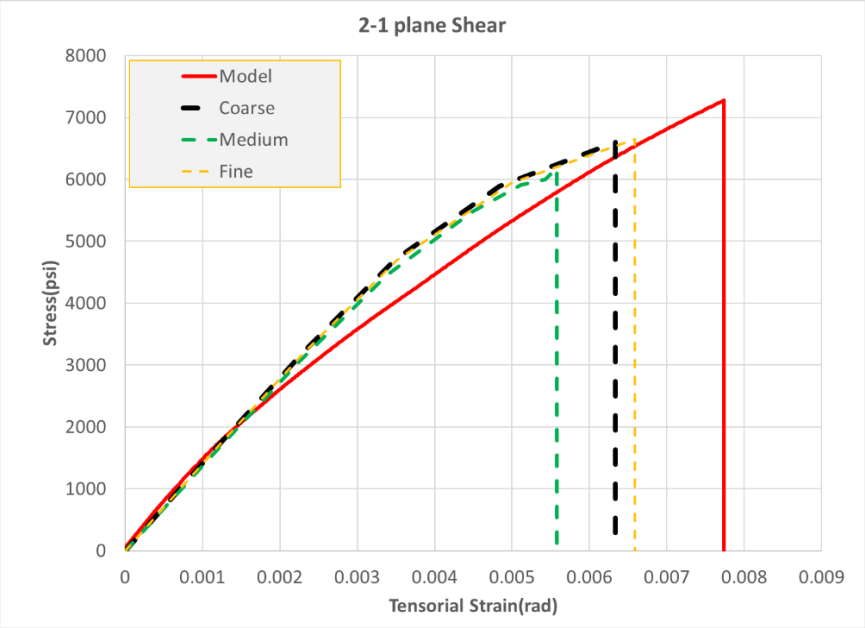


Figure 5.47 Deformation and Failure for 2-1 plane Shear Test

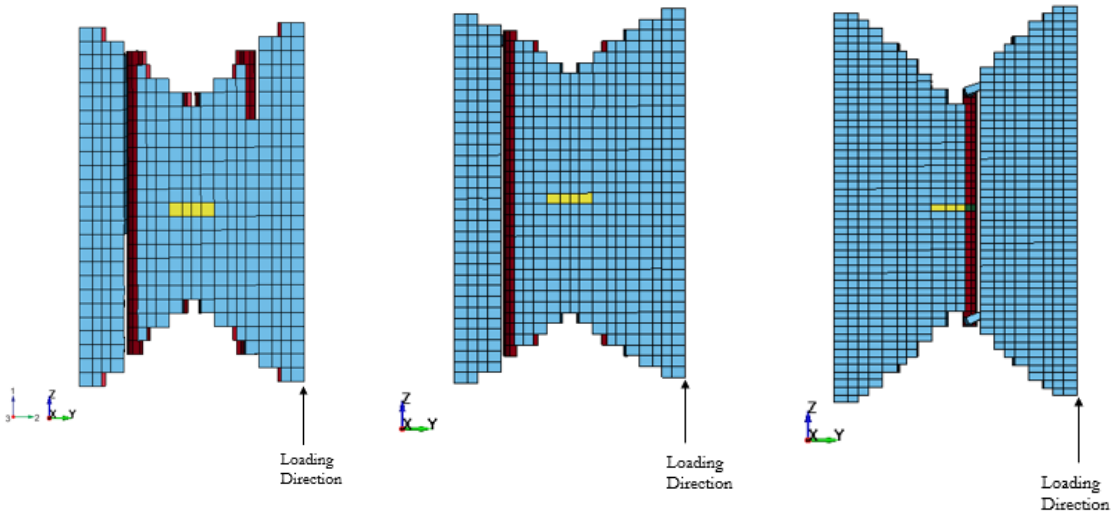


(a) (b) (c)

Figure 5.48: 2-1 plane Shear Failure in (a) Coarse Specimen (b) Medium Specimen (c) Fine Specimen

In FM, failure initiates near the top and bottom surfaces of the notch edges in the matrix elements as shown in Figure 5.49a and propagates along the fiber direction as shown in Figure 5.49b before complete failure of the specimen.

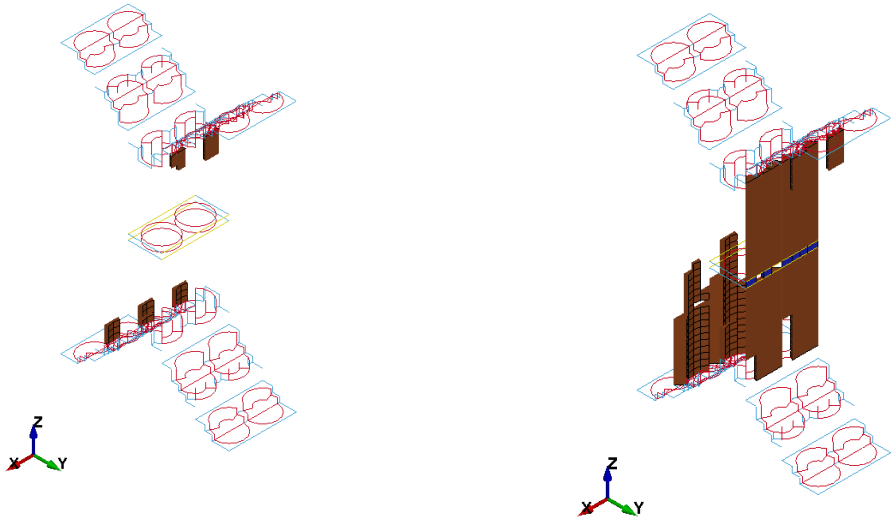


(a) (b)

Figure 5.49: 2-1 plane Shear Fine Specimen (a) Failure Initiation (b) Failure Propagation in the Matrix Elements

# CHAPTER 6

# CONCLUDING REMARKS

A virtual testing framework for unidirectional composites has been developed and discussed in this thesis. Specifically, models of the T800S/F3900 composite were built and tested using five in-plane tests in stages. First, the longitudinal compression modulus of the T800S fiber used in MAT_213 was calibrated from the virtual test of the composite in 1-direction compression. Second, the RBCFAC parameter used in MAT_187 for the F3900 matrix was calibrated through virtual tests in 2-direction compression. Finally, using the combination of the calibrated input and the experimental data for T800S carbon fiber and F3900 polymer matrix, the deformation only response of the five in-plane tests were built and tested. The deformation only response of 1-direction tension, 1-direction compression, 2-direction tension and 2-1 plane shear for all the three virtual test specimens (Coarse, Medium and Fine) showed good convergence characteristics and matched the experimental data. However, in the 2-direction compression simulation, the Coarse and the Medium specimens showed excessive deformation of the matrix elements. The excessive deformations can be attributed to the negative volume of the matrix elements under transverse compression. In the absence of refined failure-related data for the matrix element, there is excessive shearing of the matrix elements. The negative volume of the matrix elements can be avoided by artificially stiffening the material stress-strain in shear and by reducing the aspect ratio of the finite elements such that the excessive shearing of the matrix elements is reduced. The excessive deformation of the matrix elements is not observed in

the Fine Model past the *Model Curve* failure strain and failure stress thereby indicating that any mesh finer than the fine mesh and improved aspect ratio will be suitable for constructing the RUC.

The deformation and the failure response for 1-direction tension and 2-direction tension tests showed the results to be mesh independent. However, the 1-direction compression, 2-direction compression and 2-1 plane shear showed mesh sensitive results. The Fine Model specimens had the maximum ultimate strain values compared to the Coarse and Medium Model specimens. The failure in 2-direction Tension and 2-direction Compression is due to the failure in the matrix elements. The state of stress in the matrix elements for 2-direction tension is less than triaxiality of -0.33 and for 2-direction compression state of the stress is greater than triaxiality of 0.33. An approximation to the failure curve for F3900 was made for the triaxiality less than -0.33 and greater than 0.33. In the absence of experimental data, the early failure of the composite can be due to the conservative assumption of the failure curve of F3900 in case of 2-direction Tension and 2-direction Compression. Additionally, the failure of the matrix elements needs to be regularized with respect to the size of the matrix elements, since failure is mesh dependent. The mesh regularization can be done through multi-element validation of the matrix against the corresponding experimental test or failure parameters can be scaled for a given mesh to be consistent with the experimental response. The last piece in building a complete RUC is to model the fiber-matrix interface that is likely to have helped with modeling the 2-direction compression test and the 2-1 plane shear test.

With this built framework, the failure envelope can be built by first generating a virtual test specimen with an array of RUCs (similar to the illustrated PMD virtual test specimens) with appropriate boundary conditions and subjecting the test specimen to numerous in-plane states of stress. For generating the out-of-plane failure surface, the virtual tests in 3-direction tension and compression, 2-3 plane shear and 1-3 plane shear can be carried out using different RUCs employing the same FE analysis process.

# REFERENCES


[1] LSTC. LS-DYNA R11, https://lstc.com/products/ls-dyna

[2] Hoffarth C. *A generalized orthotropic elasto-plastic material model for impact analysis*. PhD Thesis, School of Sustainable Engineering & Built Environment, Arizona State University, 2016.

[3] Hoffarth C, Rajan SD, Goldberg R, Revilock D, Carney KS, DuBois P and Blankenhorn G. Implementation and validation of a three-dimensional plasticity-based deformation model for orthotropic composites. *Composites A* 2016; 91:336-350.

[4] Khaled B. *Experimental Characterization and Finite Element Modeling of Composites to Support a Generalized Orthotropic Elasto-Plastic Damage Material Model for Impact Analysis*. PhD Thesis, School of Sustainable Engineering & Built Environment, Arizona State University, 2019.

[5] Shyamsunder L, Khaled B, Rajan SD, Goldberg R, Carney K, DuBois P and Blankenhorn G. Implementing deformation, damage, and failure in an orthotropic plastic material model. *Journal of Composite Materials,* 2019. DOI:10.1177/0021998319865006.

[6] Hashin Z. Failure Criteria for Unidirectional Fiber Composites. *Journal of Applied Mechanics,* 1980; 47. DOI: 10.1115/1.3153664.

[7] Puck A and Schürmann H. Failure analysis of FRP laminates by means of physically based phenomenological models. *Composites Science and Technology*, 2002; 29. DOI: 10.1016/S0266-3538(01)00208-1.

[8] Gosse J and Christensen S. Strain Invariant Failure Criteria for Polymers in Composite Materials. *Collection of Technical Papers -AIAA/ASME/ASCE/AHS/ASC Structures, Structural Dynamics and Materials Conference*. DOI: 10.2514/6.2001-1184.

[9] Hinton MJ, Kaddour AS and Soden PD. *Failure Criteria in Fibre-Reinforced-Polymer Composites, The World-Wide Failure Exercise*. Elsevier, 2004.

[10] Goldberg R, Carney KS, DuBois P, Hoffarth C, Khaled B, Shyamsunder L, Rajan SD and Blankenhorn G. Implementation of a tabulated failure model into a generalized composite material model. *Journal of Composite Materials,* 2018. DOI: 10.1177/0021998318786778.

[11] Totry E, Gonzalez C and LLorca J. Failure locus of fiber-reinforced composites under transverse compression and out-of-plane shear. *Composites Science and Technology*, 2008; 10. DOI:10.1016/j.compscitech.2007.08.023

[12] Romanowicz M. A numerical approach for predicting the failure locus of fiber reinforced composite under combined transverse compression and axial tension. *Computational Material Science*, 2012; 5. DOI:10.1016/j.commatsci.2011.07.039.

[13] Harrington J, Hoffarth C, Rajan SD, Goldberg RK, Carney KS, DuBois P and Blankenhorn G. Using Virtual Tests to Complete the Description of a Three-Dimensional Orthotropic Material. *American Society of Civil Engineers*, 2017; 5. DOI:10.1061/(ASCE)AS.1943-5525.0000737.

[14] Toray, Toray Composite Material America Inc, [Online]. Available: www.toraycma.com

[15] Raju KS and Acosta JF. Crashworthiness of composite fuselage structures-Material dynamic properties. FAA Technical Report DOT/FAA/AR-09/8, 2010. National Technical Information Service, Springfield, VA.

[16] Asp LE, Berglund LA and Talreja R. Prediction of Matrix Initiated Transverse Failure in Polymer Composites. *Composites Science and Technology*, 1996; 8. DOI: 10.1016/0266-3538(96)00074-7.

[17] Ghorbel E. A viscoplastic constitutive model for polymeric materials. *International Journal of Plasticity*, 2008; 26. DOI: 10.1016/j.ijplas.2008.01.003.

[18] Kolling S, Haufe A, Feucht M, and DuBois P. SAMP-1: Semi Analytical Model for Simulation of Polymers. Conference: 4th LS-DYNA Anwenderforum, Bamberg, Germany, October 2005.

[19] Khaled B, Shyamsunder L, Hoffarth C, Rajan SD, Goldberg RK, Carney KS, DuBois P and Blankenhorn G. Experimental characterization of composites to support an orthotropic plasticity material model. *Journal of Composite Materials,* 2017; 25. DOI:10.1177/0021998317733319.

[20] Bednarcyk B and Arnold S. MAC/GMC 4.0 User's Manual: Keywords Manual. NASA/TM—2002-212077/VOL2. National Technical Information Service, Springfield, VA.

[21] Bogert PB, Satyanarayana A and Chunchu PB. Comparison of damage path predictions for composite laminates by explicit and standard finite element analysis tools. *47th AIAA/ASME/ASCE/AHS/ASC Structures, Structural Dynamics, and Materials Conf.*, 2006. American Institute for Aeronautics and Astronautics, Washington, DC.

[22] Robbins J. *On Building Blocks for Virtual Testing of Unidirectional Polymeric Composites.* Master's Thesis. School of Sustainable Engineering and Built Environment, Arizona State University, 2019.

[23] LSTC, LS-DYNA Keyword User's Manual, Volume II, May 2014.

[24] DuBois P, Feucht M, Haufe A, and Kolling S. A Generalize Damage and Failure Formulation for SAMP. Conference: 5th LS-DYNA Anwenderforum, Ulm, October 2006.

[25] Hu Y, Xia Z and Ellyin F. The Failure Behavior of an Epoxy Resin Subject to Multiaxial Loading. Proceedings of Pipeline Division Specialty Conference, 2006. DOI: 10.1061/40854(211)59.

[26] Khaled B, Shyamsunder L, Schimdt N, Hoffarth C, and Rajan SD. Development of a Tabulated Material Model for Composite Material Failure, MAT 213, Part 2. Experimental Tests to Characterize the Behavior and Properties of T800-F3900 Toray Composite, FAA Technical Report DOT/FAA/TC-19/50, P2,2020.